Surface Cyclolysis in the North Pacific Ocean. Part III: Composite Local Energetics of Tropospheric-Deep Cyclone Decay Associated with Rapid Surface Cyclolysis

JUSTIN G. MCLAY AND JONATHAN E. MARTIN

Department of Atmospheric and Oceanic Sciences, University of Wisconsin—Madison, Madison, Wisconsin

(Manuscript received 26 July 2001, in final form 23 April 2002)

ABSTRACT

Two regional local energetics composites of tropospheric-deep cyclone decay were constructed based upon 49 cyclones in the Gulf of Alaska region and 18 cyclones in the Bering Sea region whose decay was marked by rapid surface cyclolysis. Both composites indicate that surface drag is only a secondary sink of eddy kinetic energy (EKE) during the decay. This result holds even when a generous accounting is made for uncertainty in the surface drag calculation. The subordinate role of surface drag in the Gulf of Alaska region composite is particularly interesting, given that the cyclones in this composite decay in close proximity to rugged and extensive high-elevation terrain. Both composites also display two of the fundamental characteristics of the downstream development model of cyclone decay: the role of radiative dispersion as the chief sink of EKE during decay, and the occurrence of prominent downstream EKE dispersion. Furthermore, the two composites illustrate that an unusually pronounced decline in baroclinic conversion occurs simultaneously with the intense radiative dispersion. Taken together, these results suggest that the energetic decay of cyclones marked by rapid surface cyclolysis is driven from the upper troposphere, not from the surface.

Some notable differences also emerge from the two composites. Considerable downstream development occurs in the immediate vicinity of the decaying cyclone in the Bering Sea region composite, but not in the Gulf of Alaska region composite. Meanwhile, the areal extent of the downstream dispersion is greater in the Gulf of Alaska region composite. The latter circumstance suggests that decay events in the Gulf of Alaska region, while not producing significant downstream development in their near vicinity, may have important energetic implications for subsequent development farther downstream over North America. The composites also indicate that the decline of EKE in the vicinity of the decaying cyclone is more pronounced in the Gulf of Alaska region. In the Bering Sea region composite, this EKE is maintained via a persistent convergence of ageostrophic geopotential flux (AGF) that emanates from regions well south of the primary cyclone. Similar evidence for the influence of upstream disturbances on the cyclone decay does not appear in the Gulf of Alaska region composite.

1. Introduction

Since the introduction of the Norwegian Cyclone Model, considerable effort has been dedicated to the investigation of the cyclogenesis, mature, and occluded phases of extratropical cyclone evolution (e.g., Palmen 1951; Penner 1955; Kreitzberg 1968; Reed 1979; Shapiro and Keyser 1990; Schultz and Mass 1993; Hobbs et al. 1996; Martin 1998, 1999). A common motivation for such studies has been the association of these phases of the life cycle with the occurrence of hazardous sensible weather. Substantially less effort has been dedicated to investigating the dynamical and structural transformations associated with cyclolysis, despite its status as an integral component of the cyclone life cycle. The relatively small number of cyclolysis studies likely can be attributed to the fact that cyclone decay often heralds the *improvement* of local weather conditions, a circumstance that seemingly compels little operational urgency. What this fact may obscure, however, is that energy dispersed from decaying cyclones often initiates the growth of disturbances in the downstream direction (Orlanski and Katzfey 1991; Orlanski and Chang 1993; Chang and Orlanski 1993, 1994; Orlanski and Sheldon 1993, 1995; Chang 1993; Lee and Held 1993; Berbery and Vera 1996; Chang and Yu 1999; Chang 2000; Orlanski and Gross 2000). A central implication of such ''downstream development'' is that the precise nature of a cyclone's energetic decay may well have important consequences for the subsequent flow evolution.

Martin et al. (2001) recently constructed a continuous, long-term synoptic climatology of surface[1] cyclolysis in the North Pacific Ocean. They showed that rapid surface

Corresponding author address: Prof. Jonathan E. Martin, Department of Atmospheric and Oceanic Sciences, 1225 W. Dayton St., University of Wisconsin—Madison, Madison, WI 53706.
E-mail: jon@meteor.wisc.edu

[1] The word ''surface'' in the phrases ''surface cyclolysis'' or ''rapid surface cyclolysis'' is a colloquial reference to mean sea level.

cyclolysis occurs most frequently in two topographically distinct regions: the southern Alaska, Alexander Archipelago, and British Columbia region (hereafter the *Gulf of Alaska* region), which is characterized by extensive, high-elevation terrain; and the Bering Sea and Aleutian Island region (hereafter the *Bering Sea* region), which is characterized by much less extreme terrain. Despite the strong contrast in these two regions' terrain, it was found that rapidly decaying cyclones in both locations have quite similar tropospheric-deep structure and evolution (Marsili 2001). This observation suggests that cyclone decay associated with rapid surface cyclolysis is initiated and largely controlled by upper-tropospheric processes, not by surface drag. Verification of this suggestion is of considerable interest since it runs counter to intuition: one might reasonably expect surface drag to be the principal decay mechanism for cyclones that interact with the extreme terrain of the Gulf of Alaska region. Moreover, identification of the energetic processes that govern the decay of such cyclones would serve to indicate the extent to which this decay may influence the subsequent flow evolution (and hence sensible weather) over North America via downstream energy dispersion. Given these considerations, an assessment of the energetics of cyclone decay marked by rapid surface cyclolysis represents a meaningful and logical next step in the investigation of the cyclolysis process.

The analysis presented here is based upon local energetics composites that were constructed for 1) the Gulf of Alaska region, and 2) the Bering Sea region. All events that compose the two composites occurred during the period 1986–93. The composite diagnostics were derived using an eddy and time-mean flow methodology coupled with local energetics. The study is organized as follows. Section 2 provides an overview of the current understanding of the energetics of cyclone decay. The local energetics approach and the data used in the study are outlined in section 3. The composite vertically averaged diagnostics for the Gulf of Alaska region are presented in section 4, and those for the Bering Sea region are presented in section 5. Discussion and conclusions follow in section 6.

2. Background

Prior work concerning the energetics of cyclone decay has focused on three primary decay mechanisms: barotropic conversion, downstream dispersion, and frictional dissipation. Here, a brief review is given of each of these mechanisms, with barotropic conversion being considered first.

a. Barotropic conversion

In his work on the atmospheric energy cycle Lorenz (1955) noted that the maintenance of the observed general circulation requires that atmospheric eddies must eventually transfer some of their kinetic energy to the mean flow. In a spatially or temporally averaged framework this transfer primarily involves an interaction of horizontal eddy momentum fluxes with the horizontal shear of the mean flow. Specifically, when the eddy momentum components are positively (negatively) correlated equatorward (poleward) of the mean jet, energy is transferred from the eddies to the mean flow. Such a transfer is identified as being ''barotropic'' and leads to the so-called barotropic decay of eddies. As an example, negatively tilted upper-tropospheric troughs that are located poleward of the mean jet are subject to barotropic decay.

Simons (1972) investigated the instability of large-scale wave perturbations on a zonal current using linear and nonlinear integrations of a quasigeostrophic, adiabatic, and inviscid spectral model. He found that barotropic transfer of kinetic energy between the eddies and the zonal mean flow became very significant as the eddy kinetic energy reached an order of magnitude comparable to that of observed atmospheric waves and as the eddies' baroclinic growth decreased.

Simmons and Hoskins (1978), using a 3D primitive equation spectral model to investigate the nonlinear evolution of normal mode perturbations to a balanced zonal flow, found that a barotropic conversion of eddy kinetic energy to zonal kinetic energy became dominant as baroclinic growth of the disturbances diminished. In subsequent work, Simmons and Hoskins (1980) emphasized the role of mean flow shear and the corresponding kinetic energy conversion between the eddy and the mean flow in the life cycle of baroclinic waves. They showed that the addition of a barotropic zonal wind component to the flow produced marked variations in the area-averaged eddy kinetic energy (EKE) evolution of normal mode perturbations to the flow.

Thorncroft et al. (1993) demonstrated the effect of added barotropic meridional cyclonic/anticyclonic shear on the area-averaged EKE evolution of baroclinic waves in 3D primitive equation spectral model simulations on a sphere. The case with added cyclonic shear, life cycle 2 (LC2), exhibited larger, more persistent EKE values than the case with added anticyclonic shear (life cycle 1, or LC1). In the LC1 case their model results indicated strong barotropic decay of the waves' EKE.

Balasubramanian and Yau (1996) investigated moist and dry simulations of the life cycle of a marine cyclone from an energetics perspective using a hydrostatic, primitive equation channel model with beta-plane geometry and periodic east–west boundary conditions. The decay stage of the cyclone in both the moist and dry simulations was marked by a decrease in EKE arising from strong barotropic exchange of energy between the eddy and the zonal-mean flow.

Closely related to the barotropic decay process is the concept of a ''barotropic governor.'' Introduced by James and Gray (1986), the barotropic governor describes a positive feedback between horizontal shear of the basic-state flow and eddy momentum fluxes that limits an eddy's growth and results in its eventual bar-

otropic decay. James (1987) offered the barotropic governor as an explanation for how horizontal shear of the basic state reduced the growth rate of unstable normal modes in a linear, two-level baroclinic channel model on a beta plane. The influence of the barotropic governor was confirmed by Davies et al. (1991) in work that examined the growth of normal mode perturbations to a symmetric baroclinic jet using a semigeostrophic 3D spectral model, and by Nakamura (1993) in an investigation of normal mode evolution in the presence of barotropic basic state shear using quasigeostrophic and primitive equation models. Mak (2000) further suggested the importance of the barotropic governor, citing its role in the evolution of unstable normal mode perturbations to a zonal jet within a 3D quasigeostrophic channel model. The aforementioned results all suggest that barotropic transfer of EKE to mean flow kinetic energy is a primary mechanism of eddy decay.

b. Downstream dispersion

A second mechanism of local eddy energy decay that has been cited by prior studies is downstream energy dispersion. Kung (1977) suggested the importance of dispersive energy fluxes in the kinetic energy budget of many midlatitude synoptic-scale waves. Later, Mak and Cai (1989), using barotropic, nondivergent channel model simulations, suggested that pressure work, which is closely related to energy fluxes, is one of the three primary mechanisms governing the growth and decay of modal and nonmodal disturbances.

Orlanski and Katzfey (1991) examined the energetics of a Southern Hemisphere cyclone wave and found that the primary EKE sink was the ageostrophic geopotential flux (AGF), which arises from the pressure work terms in the governing equations. They reconciled their results with those of the normal mode studies, where barotropic processes dominate the eddy decay, by citing the fact that ageostrophic fluxes into and out of individual normal modes exhibit an exact balance so that the net integrated flux acting on the normal mode is zero.

In an idealized modeling study of the importance of AGF, Orlanski and Chang (1993) showed that downstream fluxes of eddy energy were instrumental in promoting eddy decay and were significant contributors to subsequent eddy development downstream. A synopsis of this ''downstream baroclinic evolution,'' wherein the decay of cyclones in a wave train occurs primarily through downstream ageostrophic fluxes of energy, was presented by Orlanski and Sheldon (1995).

Recently, Chang (2000) performed a study of wave packets and trough life cycles observed during a single Southern Hemisphere summer season. He computed EKE budgets for the life cycles of individual troughs associated with two distinct wave packets and found that, during the decay phase of a majority of these troughs, downstream dispersion of energy was the dominant mechanism. A similar finding was made for the limited set of troughs (not necessarily associated with the wave packets) displaying the most significant geopotential height fall or EKE maximum. However, while AGF was most frequently the dominant decay mechanism within these two sets of troughs, Chang also notes that a not insignificant number of the troughs decayed primarily through barotropic processes or frictional dissipation.

c. Frictional dissipation

A limited number of studies have demonstrated that subgrid-scale dissipation (which may include both surface drag and internal dissipation, but which is often referred to collectively as frictional dissipation) may be a leading sink of kinetic energy in extratropical cyclones. Smith (1973) analyzed the kinetic energy budgets of the prestorm, growth, and decay stages of an intense cyclone over North America. A volume-integrated kinetic energy budget for the immediate storm vicinity, averaged over the period spaning the cyclone's growth and decay, indicated that dissipation was the most prominent sink. Additionally, Robertson and Smith (1980) analyzed the kinetic energy budgets of two extratropical cyclones over North America and found that dissipation (determined as a residual) became the dominant sink of kinetic energy during the latter stages of one of the storms.

The composite kinetic energy budgets for five distinct stages of extratropical cyclone development were analyzed by Masters and Kung (1986). They showed that dissipation (determined as a residual) was minimal during the incipient stage of the cyclones but progressively increased to become the dominant sink of kinetic energy by the occluded stage of the cyclones.

Chang (2000) computed EKE budgets for the life cycles of 20 troughs observed during a single Southern Hemisphere summer season and found that frictional dissipation (determined as a residual) dominated the decay phase of 1 in 10 of these troughs. Comprehensive budget diagnostics were also presented for troughs associated with a distinct, long-lived wave packet that was observed during the season. Frictional dissipation (determined as a residual) was found to make significant but not dominant contributions to the decay of 7 of the 10 troughs related to the wave packet.

3. Data and methodology

a. Data

The two local energetics composites described in this study were constructed using European Centre for Medium-Range Weather Forecasts (ECMWF) reanalysis data. Discretized reanalyses are available in the form of global 2.5° latitude–longitude grids at the surface and at 17 unequally spaced pressure levels. Reanalysis variables used in the course of this work include the geo-

potential (ϕ), the horizontal wind components (u, v), isobaric vertical velocity (ω), mean sea level pressure (SLP), surface pressure (P_s), zonal surface stress (τ_{si}), meridional surface stress (τ_{sj}), and the 10-m horizontal wind components (u_0, v_0). The composite diagnostics were created using daily 0000 and 1200 UTC reanalyses for the six months of October–March during the time period 1986–93. Reanalysis data were acquired from the National Center for Atmospheric Research (NCAR) in gridded binary (GRIB) format and then transferred to General Meteorological Analysis Package (GEMPAK) grids with cylindrical equidistant (CED) grid projection. The GEMPAK grids were accessed by independent programs for the performance of diagnostic computations.

The use of these global analyses entails several limitations. The resolution of the data is relatively coarse both spatially and temporally and this limits the accuracy of any diagnostic computations that are performed. Coarse temporal resolution also conceals all but the most prominent details of temporal variation. Furthermore, the analyses are dependent upon only one global model and will thus reflect the biases inherent within that model. Though such biases do not necessarily imply that the analyses are incorrect, they nevertheless underlie any diagnostic computations that are performed using the analyses [see Chang (2000) for a more extensive discussion of this topic]. Limitations such as these are of some concern. However, the large spatial domain and long time periods involved in this work necessitate the use of the analyses from a practical standpoint.

b. Local energetics

Central to the local energetics approach is the application of an Eulerian time-tendency equation for eddy kinetic energy (EKE). Use of this equation offers several advantages. For one, assessment of the eddy component of the total kinetic energy serves to emphasize the significant transient variations in a flow's kinetic energy. Also, the EKE tendency equation provides a comprehensive and unambiguous framework for diagnosing the mechanisms responsible for changes in EKE. Furthermore, the equation allows for the investigation of individual cyclones and provides a convenient vehicle for analyzing interaction between upstream and downstream disturbances. The definition of the EKE follows from a partitioning of the instantaneous wind velocity into time-mean and eddy components as

$$\mathbf{V} = \overline{\mathbf{V}} + \mathbf{V}',$$

where

$$\overline{\mathbf{V}} = \overline{u}\hat{i} + \overline{v}\hat{j} + \overline{\omega}\hat{k},$$
$$\mathbf{V}' = u'\hat{i} + v'\hat{j} + \omega'\hat{k},$$

and the ($\bar{}$) indicates a time-mean quantity. The instantaneous horizontal EKE per unit mass is then

$$K_e = \frac{u'^2 + v'^2}{2}.$$

A partitioning of the geopotential (Φ) and aerodynamic stress vector (τ) into mean and eddy components as

$$\Phi = \overline{\Phi} + \phi' \quad \text{and} \quad \tau = \overline{\tau} + \tau',$$

and the definition of the mean and eddy horizontal velocity vectors as

$$\overline{\mathbf{V}}_\mathbf{h} = \overline{u}\hat{i} + \overline{v}\hat{j} \quad \text{and} \quad \mathbf{V}'_\mathbf{h} = u'\hat{i} + v'\hat{j}$$

allows the EKE tendency equation to be obtained in spherical and isobaric coordinates from the primitive horizontal momentum equations and the continuity equation as

$$\underset{\text{a}}{\frac{\partial K_e}{\partial t}} = \underset{\text{b}}{-\boldsymbol{\nabla}_3 \cdot \mathbf{V}K_e} \underset{\text{c}}{- \mathbf{V}'_\mathbf{h} \cdot (\mathbf{V}' \cdot \boldsymbol{\nabla}_3)\overline{\mathbf{V}}_\mathbf{h}} \underset{\text{d}}{+ u'(\overline{\boldsymbol{\nabla}_3 \cdot u'\mathbf{V}'})} \underset{\text{e}}{+ v'(\overline{\boldsymbol{\nabla}_3 \cdot v'\mathbf{V}'})} \underset{\text{f}}{+ \frac{\tan\psi}{r}[u'u'\overline{v} - u'v'\overline{u} - u'\overline{u'v'} + v'\overline{u'u'}]}$$
$$\underset{\text{g}}{+ \omega'\frac{\partial \phi'}{\partial P}} \underset{\text{h}}{- \boldsymbol{\nabla}_3 \cdot \mathbf{V}'\phi'} \underset{\text{i}}{- g\frac{\partial}{\partial P}(\mathbf{V}'_\mathbf{h} \cdot \tau')} \underset{\text{j}}{+ \text{res.}} \tag{1}$$

Here ψ is latitude, P is pressure, r is the radius of the earth, and g is the gravitational acceleration. The derivation of Eq. (1) is provided in appendix A. Interpretation of the individual terms in (1) is as follows. Other variations on the EKE tendency equation are presented and interpreted by Orlanski and Katzfey (1991), Lackmann et al. (1999), and Chang (2000).

Term a, on the left-hand side of (1), is the observed local time tendency of EKE. This term is obtained by summation of all terms on the right-hand side (rhs) of (1).

Term b, on the rhs of (1), is the advective flux divergence term. It describes the advection of EKE by the total flow, and its net effect is to shift EKE downstream relative to the direction of the total flow. Advective flux divergence does not remove from or add to the flow any EKE, nor does it radiatively disperse EKE within the flow.

Term c on the rhs of (1) is the shear generation term and describes the interaction of instantaneous eddy momentum fluxes (Reynolds stresses) with gradients in the mean wind. Shear generation is regarded as a barotropic mechanism of growth or decay since in the classical Lorenz time-averaged energetics it reflects a direct transfer of kinetic energy between the eddy and the mean flow and this transfer largely involves horizontal gradients in the mean flow. In the instantaneous time frame of local energetics the energy transfer is between eddy kinetic energy and that portion of the total kinetic energy contained in the correlation of eddy and mean velocity components. Despite this distinction, the interpretation of shear generation as a barotropic mechanism remains fundamentally valid.

Terms d and e on the rhs of (1) will be referred to as the zonal and meridional momentum correlation, respectively, since they are defined by the correlation of an eddy wind component with the mean divergence of the eddy flux of that component. The operation of these terms can be understood by first recalling that mean eddy momentum flux divergence/convergence imparts changes to the basic-state momentum that are accompanied by opposite changes in eddy momentum. The sign of the eddy momentum determines whether these changes lead to an increase or decrease in the magnitude of the eddy momentum and, thereby, to an increase or decrease in EKE. Hence the presence in (1) of correlations between mean eddy momentum flux divergence/convergence and eddy momentum. These terms, like the shear generation term, largely involve the interaction of an eddy variable with horizontal shear of another quantity and can be regarded as a barotropic source or sink of EKE. More precisely, they signify a conversion between eddy kinetic energy and the kinetic energy of the correlation of eddy and mean velocity components.

Term f on the rhs of (1) is the curvature term and represents the impact of spherical geometry on the EKE evolution. The curvature of the earth's surface implies that the directions of the local coordinate axes vary with location on the earth's surface. Flow relative to the surface of the earth will thus experience an acceleration associated with the change in direction of the local coordinate axes. The flow's acceleration varies as the product of the speed of the flow and the rate of variation in direction of the local coordinate axes. The change in momentum of the flow is reflected in a change in the flow's kinetic energy.

Term g on the rhs of (1) is the baroclinic conversion and represents the conversion of eddy available potential energy to eddy kinetic energy. Term h on the rhs of (1) is the radiative flux divergence term. It describes the dispersion of EKE within the flow by pressure work, and is referred to with the qualifier ''radiative'' in order to emphasize the nonadvective nature of the flux divergence. Chang and Orlanski (1994) have provided observational evidence that the horizontal radiative energy flux

$$\mathbf{V}'_{\mathbf{h}}\phi' \equiv (u'\phi')\hat{i} + (v'\phi')\hat{j} \tag{2}$$

when modified by subtraction of a specific nondivergent vector

$$\hat{k} \times \nabla \frac{\phi'^2}{2f}$$

provides a reasonable estimate of the direction of the dispersive energy flux that occurs within nonlinear and baroclinic disturbances. The resultant flux

$$(\mathbf{V}'_{\mathbf{h}}\phi')_a = \mathbf{V}'_{\mathbf{h}}\phi' - \hat{k} \times \nabla \frac{\phi'^2}{2f} \tag{3}$$

was named the ageostrophic geopotential flux, or AGF, by Orlanski and Katzfey (1991). AGF vectors are a convenient and powerful tool for analyzing the energetic interaction of various disturbances within a flow.

Term i on the rhs of (1) describes the vertical flux divergence of the rate of work by aerodynamic stress. Similar terms that describe the horizontal flux divergence of the rate of work by aerodynamic stress also could be represented. However, these terms make relatively small contributions on the scales resolved by the global analyses and, so, are included in the residual term rather than explicitly represented. Term i can be considerably simplified through vertical integration, with the fairly good assumption that the aerodynamic stress becomes relatively insignificant toward the top of the domain. With this assumption, the vertical integral of term i between the surface and 100 hPa can be approximated as

$$\int_{100}^{P_s} -g\frac{\partial}{\partial P}(\mathbf{V}' \cdot \tau')\, dP$$
$$= -g((\mathbf{V}' \cdot \tau')|_{P_s} - (\mathbf{V}' \cdot \tau')|_{100}) \approx -g(\mathbf{V}' \cdot \tau')|_{P_s}. \tag{4}$$

Thus, the vertical integral of term i is dependent only upon the rate of work done by the surface aerodynamic stress, a process that can more simply be referred to as the surface drag. Since in this study term i was only evaluated as a vertical average, it is hereafter referred to as the ''surface drag'' term. It is important to note that here, owing to the particular surface stress formulation used by ECMWF, the surface drag term is a measure of both drag due to unresolved turbulent vertical momentum flux and pressure (or form) drag due to flow around unresolved mountainous topography (Lott 1995).

The residual, term j on the rhs of (1), is the difference between the observed tendency of EKE (term a) calculated directly from the ECMWF analyses and the diagnosed tendency of EKE given by the summation of terms b–i on the rhs of (1). The residual measures the cumulative effect of all the processes that are not explicitly represented on the rhs of (1). Included in the residual are the effects of internal viscous dissipation,

of gravity wave stress, and of horizontal flux divergence of the rate of work by surface stress, as well as the effects of finite-difference, integration, and interpolation errors. Also, the assimilation process may introduce a nonphysical increment in the value of the analysis variables between successive analyses, and the effect of this increment is included in the residual. The method used for evaluating the residuals at a particular analysis time t is described in appendix B.

For diagnostic computations involving (1), the time mean was assumed invariant and was defined over the period consisting of the 6 months from October through March. This period was selected because, being the winter season, it encompasses the peak of cyclolytic activity in the North Pacific Ocean region (Martin et al. 2001). Time means were determined for each of the seven October–March periods that are contained within the time span from 1986 through 1993.

Equation (1) was discretized with second-order finite differences in both the horizontal and vertical directions. Computations were performed on the global analyses' latitude–longitude grid, and only at grid points above the surface.[2] Computations were further limited to those locations in the Northern Hemisphere between 10° and 87.5°N.

This study focuses on analysis of the composite vertically averaged tendency terms, where the vertical average for any variable A is defined as

$$\frac{1}{(P_s - P_t)} \int_{P_t}^{P_s} A \, dP$$

and P_s = surface pressure and P_t = 100 hPa. Analysis of the vertical average, rather than the vertical integral, avoids problems in interpretation that might arise in association with the variation of the integration interval with surface pressure. Vertical integration was performed by first interpolating those values located above the surface to equally spaced (at 50-hPa intervals) pressure levels. After interpolation, integration was completed using the trapezoidal rule over the pressure interval adjacent to the surface and Simpson's rule over the remaining pressure intervals. For the integration, surface values of the tendency terms were obtained through polynomial extrapolation of values at higher levels.

c. Composite definitions and methodology

The local energetics regional composites were constructed based upon North Pacific Ocean cyclones that, during decay, exhibited at least one rapid surface cyclolysis period (RCP), defined as a 12-h period during which the surface cyclone's mean sea level pressure minimum rises by at least 12 hPa (Martin et al. 2001). For the purposes of this study, a surface cyclone is defined as a minimum in the SLP field surrounded by at least one closed isobar (analyzed at 2-hPa intervals). The composite for cyclones that occurred in the Gulf of Alaska region was constructed from 49 distinct cyclones. For reference, the positions of these storms' SLP minima at the beginning of their respective RCPs are shown in Fig. 1a. The composite for cyclones that occurred in the Bering Sea region was constructed from 18 distinct cyclones. Figure 1b shows the positions of these storms' SLP minima at the beginning of their respective RCPs.

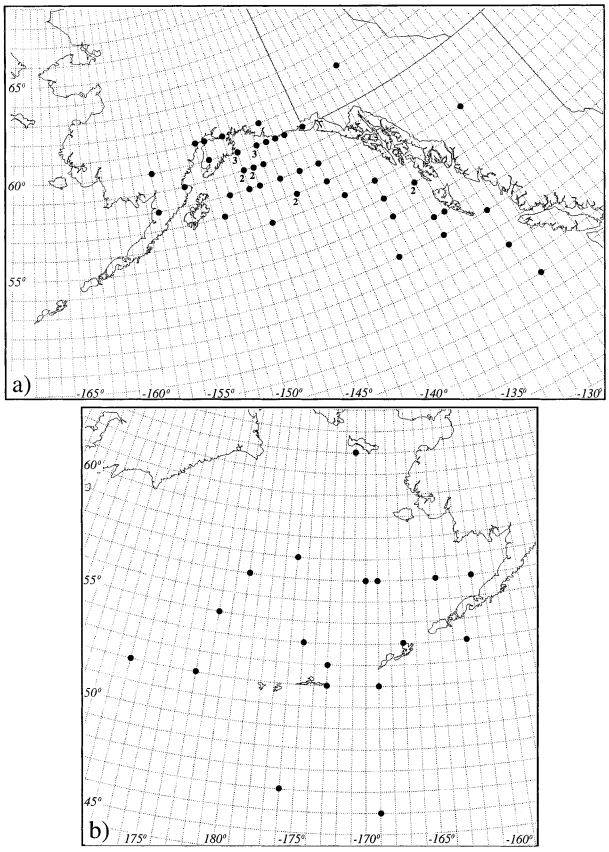

FIG. 1. (a) Dots represent the locations at $T = 0$ of the SLP minima of cyclones included in the Gulf of Alaska region composite. Some locations experienced more than one qualifying cyclone during the period 1986–93. The number of cyclones at each such location is indicated by the number adjacent to the dot. (b) As in (a) but for the Bering Sea region composite.

For each cyclone in the composites, the analysis time $T = 0$ is defined as the beginning of the 12-h period that marked the first RCP for the given cyclone. This designation allows the discussion of the composite local energetics diagnostics to reference a common decay-following time. In the course of the subsequent presentation reference will be made to three other analysis times: $T - 24$, $T - 12$, and $T + 12$, which refer to the

[2] Horizontal finite-difference computations were also restricted only to those locations where all grid points forming the horizontal finite-difference stencil were above the surface.

moments 24 and 12 h before, and 12 h after, the initiation of rapid decay, respectively.

Construction of the composites first involved the definition of a composite grid. This fixed grid was chosen to have dimensions (in meters) equivalent to those of a 40° latitude × 90° longitude domain centered at 40°N. Selection of these dimensions ensured that the composite grid would encompass features and activity well upstream and downstream of each cyclone included in the composite. Also, these dimensions imply that the domain of the composite grid has a trapezoidal shape, where the northernmost grid row is shorter (in meters) than the southernmost grid row. The motivation for selecting this shape for the grid is outlined in step 3 below. Additionally, the grid is defined to have a fixed number of grid points in the zonal and meridional directions (37 and 17 points, respectively), meaning that the distance separating the grid points in the zonal direction is a function of grid row. The distance separating the grid points in the meridional direction is a constant, equivalent to the distance in meters associated with a 2.5° increment in latitude. Having defined the composite grid, the following procedure was then used for the case-by-case construction of the composites. For a given cyclone and analysis time,

1) all local energetics diagnostics (both those at discrete pressure levels and those in vertically averaged form) were calculated on the ECMWF latitude–longitude grid;
2) the ECMWF grid point closest to the location of the cyclone's sea level pressure minimum was determined;
3) the grid point determined in step 2 was taken to represent the center of the composite grid. The composite grid was then ''overlain'' on the ECMWF latitude–longitude grid such that a given row of the composite grid was superimposed with a given row of the ECMWF grid. The overlay process sometimes entailed the superposition of the northernmost grid rows of the composite grid with ECMWF grid rows of very high latitude. In order to ensure that, in this event, overlap of points toward the east and west ends of the composite grid would not occur, the construction of the composites involved (a) adoption of the trapezoidal shape for the composite grid and (b) exclusion from the composite of cyclones whose sea level pressure minima were at any time located north of 63°N; and
4) a particular grid point on the composite grid was selected. The closest ECMWF grid point to the east of this composite grid point was located, as was the closest ECMWF grid point to the west of this composite grid point. The values of the local energetics diagnostics at these ECMWF grid points were then used in linear interpolation to obtain values of the local energetics diagnostics at the composite grid point. This step was repeated for all composite grid points.

After completing steps 1–4 for all cyclones at a particular analysis time, the composite distribution at that analysis time of a given local energetics variable for the Gulf of Alaska region (Bering Sea region) was then constructed by taking the 49-cyclone (18 cyclone) average of that variable at each of the grid points within the composite grid. Contours of the composite variables are displayed within the composite grid's equivalent form, a 40° latitude × 90° longitude domain centered at 40°N, in a polar stereographic projection.

4. Gulf of Alaska region composite local energetics diagnostics

a. Vertically averaged EKE evolution

Analysis of the composite vertically averaged EKE evolution begins at the analysis time $T - 24$. At this time the composite cyclone is associated with a well-developed and slightly negatively tilted trough in the 300-hPa geopotential height (Fig. 2a). Downstream of the primary trough and to the distant southeast of the SLP minimum is a second, smaller-amplitude trough (hereafter referred to as the downstream trough). The most prominent EKE maximum at this time is located along the downstream flank of the primary trough. This primary EKE maximum is located immediately to the southeast of the SLP minimum and forms the northern portion of a broad, comma-shaped EKE feature. The EKE downstream of the primary trough is of a fairly uniform and weak magnitude and exhibits a single, modest maximum in the vicinity of the downstream trough.

At $T - 12$ the height pattern is similar except for the slightly more negative tilt of the northern portion of the primary trough (Fig. 2b). Meanwhile, the prominent, comma-shaped EKE feature observed at $T - 24$ has evolved into a meridionally elongated feature that is located entirely along the downstream flank of the primary trough. The cyclone's primary EKE maximum continues to form the northern part of this feature, and remains located immediately to the southeast of the SLP minimum. This primary EKE maximum has not experienced a significant change in magnitude. The southern part of the meridionally elongated EKE feature is marked by another maximum, which is smaller but as intense as the primary maximum. Also of note, the EKE maximum in the vicinity of the downstream trough has increased in size but remains of a comparatively weak magnitude.

At $T = 0$ the northern portion of the primary trough maintains a strong negative tilt (Fig. 2c). However, this trough and the ridge to its east have experienced a modest decrease in amplitude. Regarding the EKE, the most notable detail at this time is the much reduced intensity of the EKE feature on the downstream flank

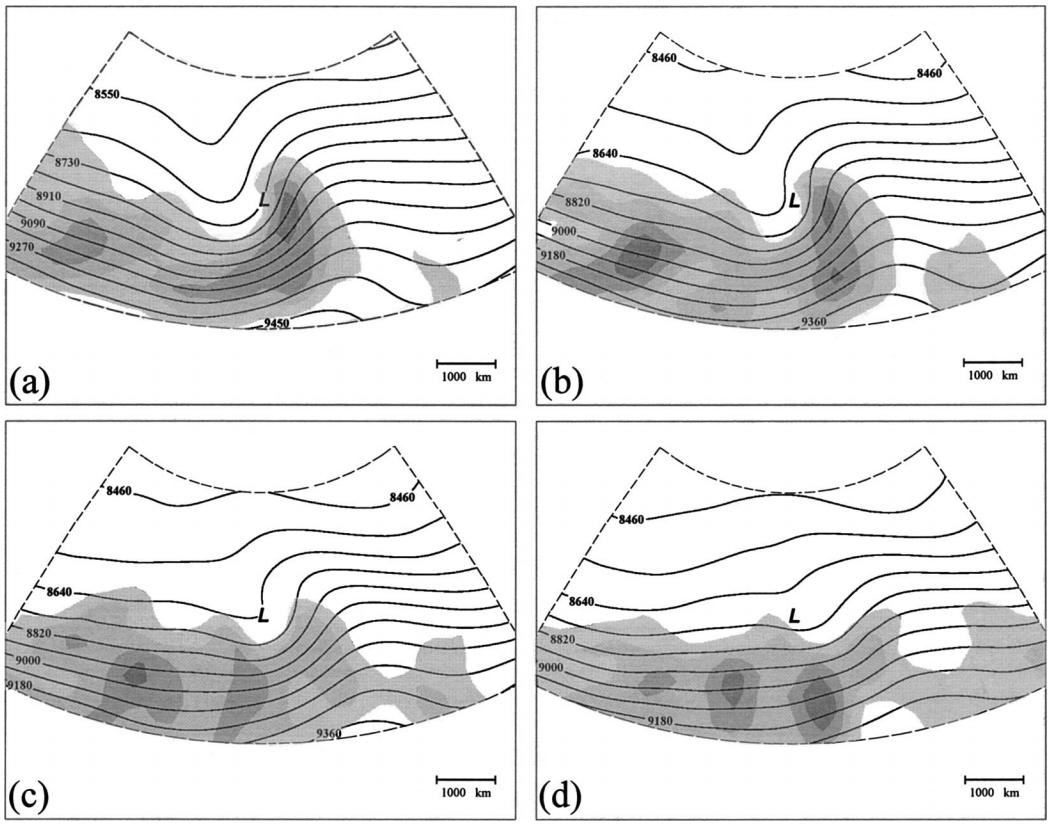

FIG. 2. (a) Gulf of Alaska region composite vertically averaged EKE and 300-hPa geopotential height at $T - 24$. EKE is shaded every 30 $m^2\ s^{-2}$ beginning at 150 $m^2\ s^{-2}$. Geopotential height is labeled in dam and contoured every 9 dam. Bold L represents the position of the SLP minimum. Approximate length scale indicated in lower-right corner. Long dashed lines are latitude and longitude bounds of the composite grid (see text for explanation) spaced by 40° and 90°, respectively. (b) As in (a) but for time $T - 12$. (c) As in (a) but for time $T = 0$. (d) As in (a) but for time $T + 12$.

of the primary trough. This feature is now only of moderate magnitude and no longer possesses significant maxima. Furthermore, the feature has shifted eastward relative to the SLP minimum. Elsewhere, modest intensification of the EKE maximum associated with the downstream trough has occurred. In addition, a notable and meridionally elongated EKE maximum is now present along the southern portion of the primary trough's upstream flank.

By $T + 12$ the primary trough has moved downstream of the SLP minimum and its amplitude has dramatically decreased (Fig. 2d). Most important, the EKE on the downstream flank of the primary trough is now minimal except near the trough's base. Intense EKE can, however, be found to the south of this trough (to the distant south-southeast of the SLP minimum), in association with the EKE maximum that was formerly located along the southern portion of the primary trough's upstream flank. A lesser EKE maximum at the very southeast corner of the composite grid is the only EKE feature of note downstream of the primary trough.

b. Vertically averaged local energetics tendency terms

A composite was created for the vertical average of each term on the rhs of (1) as well as the related vertically averaged AGF vectors. With one exception, only those terms that achieve a ''first order'' magnitude [$O(10^{-3})$ or higher] at some time during the analysis period are described in the discussion that follows. Also, the vertically averaged radiative flux divergence term to which reference is made in the following discussion is based on the three-dimensional radiative energy flux divergence term presented in (1). This means that it includes contributions from both horizontal and vertical radiative flux divergence. Analysis indicates, however, that the vertically averaged horizontal radiative energy flux divergence makes the dominant contributions. Thus, the vertically averaged three-dimensional radiative flux divergence and the vertically averaged horizontal ageostrophic flux vectors can be expected to provide consistent indications of radiative flux divergence. Furthermore, the secondary contributions made by the

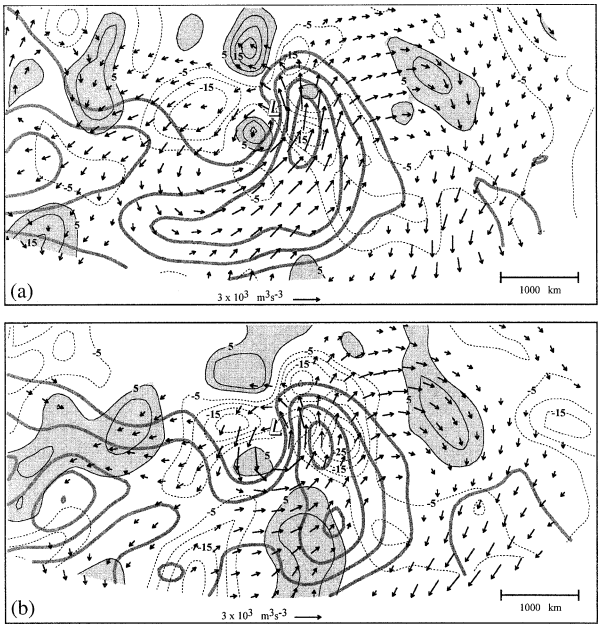

FIG. 3. (a) Gulf of Alaska region composite vertically averaged AGF vectors, radiative flux divergence term ($-\nabla_3 \cdot \mathbf{V}'\phi'$), and EKE at time $T - 24$. AGF vectors are solid arrows in units of $m^3\ s^{-3}$ with reference arrow indicated. Thin solid (dashed) lines are positive (negative) values of the radiative flux divergence term labeled in $10^{-4}\ m^2\ s^{-3}$ and contoured every $5 \times 10^{-4}\ m^2\ s^{-3}$ ($-5 \times 10^{-4}\ m^2\ s^{-3}$) beginning at $5 \times 10^{-4}\ m^2\ s^{-3}$ ($-5 \times 10^{-4}\ m^2\ s^{-3}$). Positive values of the radiative flux divergence term are shaded. Thick gray solid lines are vertically averaged EKE contoured every $30\ m^2\ s^2$ beginning at $150\ m^2\ s^2$. Outlined L represents the position of the sea level pressure minimum. Approximate length scale indicated in lower-right corner. (b) As in (a) but for time $T - 12$.

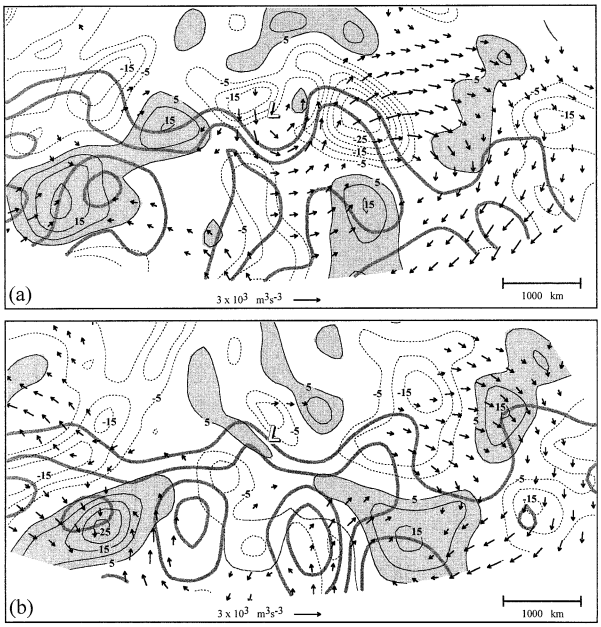

FIG. 4. (a) As in Fig. 3a but for time $T = 0$. (b) As in Fig. 4a but for time $T + 12$.

vertically averaged vertical radiative flux divergence justify dispensing with separate descriptions of the vertically averaged horizontal and vertical radiative flux divergence.

In Fig. 3 (Fig. 4) the vertically averaged AGF vectors and radiative flux divergence term are plotted with the composite vertically averaged EKE and the position of the sea level pressure minimum at times $T - 24$ and $T - 12$ ($T = 0$ and $T + 12$). At $T - 24$, significant AGF emanates from the downstream[3] nose of the primary EKE maximum in a radial manner, such that a well-defined AGF extends not only downstream but in other directions ranging from northward through westward (Fig. 3a). The emanation is predominantly marked by radiative flux divergence, while there is radiative flux convergence to the northwest of the EKE maximum and a broad, weak region of convergence immediately downstream. The downstream AGF emanating from the primary EKE feature is particularly extensive. Its trajectories trace out a long, anticyclonically curved path that runs first eastward and then well to the south and southwest. In contrast, the magnitude of the northward AGF tends to diminish rapidly with distance. Much of the AGF that emanates westward from the primary EKE feature eventually coalesces into a southwestward AGF some distance to the west of the SLP minimum, or is incorporated into an asymmetric AGF vortex that is centered close to this minimum. Divergence is prevalent in the AGF that forms the western flank of this vortex while weakly divergent AGF predominates over the vortex's southern flank.

At $T - 12$, the extensive downstream AGF from the primary EKE feature's eastern flank prevails (Fig. 3b). Also notable is the more intense radiative flux divergence that envelopes much of the primary EKE feature. An AGF vortex remains centered close to the SLP minimum and a southwestward AGF from the vortex's western flank, though less pronounced, is still discernable. Broad regions of flux convergence are now evident to the west of the primary EKE feature and along this feature's southern flank.

At $T = 0$ vigorous downstream AGF from the cyclone's downstream flank and associated intense flux divergence are the preeminent features (Fig. 4a). The flux divergence that operates with respect to the primary EKE feature is extensive and even more intense than 12 h prior. Also, the lengthy trajectories of the downstream AGF persist, though ultimately some of these trajectories now terminate in an area of flux convergence to the distant southeast of the SLP minimum. Meanwhile, the AGF vortex that had been centered near the sea level pressure minimum, as well as the southwestward AGF that emanated from the western flank of this vortex, are no longer prominent.

[3] The downstream and upstream directions are defined relative to the *total* (mean + eddy) flow, unless otherwise stated. Refer to Fig. 2 for a sense of the orientation of the total flow.

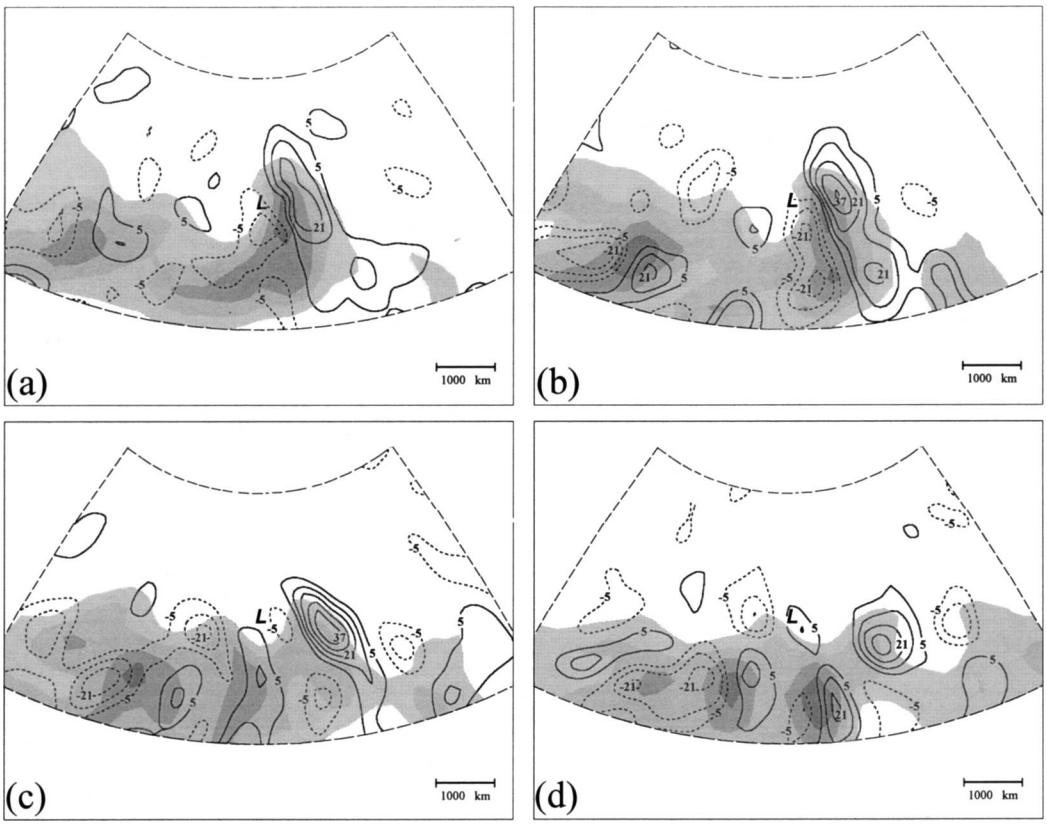

FIG. 5. (a) Gulf of Alaska region composite vertically averaged advective flux divergence term and EKE at time $T - 24$. Solid (short dashed) lines are positive (negative) values of the advective flux divergence term labeled in 10^{-4} m^2 s^{-3} and contoured every 8×10^{-4} m^2 s^{-3} (-8×10^{-4} m^2 s^{-3}) beginning at 5×10^{-4} m^2 s^{-3} (-5×10^{-4} m^2 s^{-3}). EKE shaded as in Fig. 2. Bold L represents the position of the SLP minimum. Approximate length scale indicated in lower-right corner. Latitude and longitude are as in Fig. 2. (b) As in (a) but for time $T - 12$. (c) As in (a) but for time $T = 0$. (d) As in (a) but for time $T + 12$.

By $T + 12$, AGF in the vicinity of the SLP minimum has markedly declined (Fig. 4b). However, notable downstream AGF can still be found emanating from the cyclone's far eastern flank. The corresponding flux divergence remains significant but the maximum values are much reduced from those 12 h earlier. Additionally, more intense flux convergence is now present along the trajectories of the downstream AGF, and the maximum in flux convergence to the distant southeast of the SLP minimum is broader.

The composite advective flux divergence term is shown together with the vertically averaged EKE in Fig. 5 at each of the analysis times. Through $T = 0$ the advective flux divergence induces first-order positive local time tendencies of EKE along the eastern side of the primary EKE feature and negative tendencies along that feature's western side. By $T + 12$ the negative tendencies along the cyclone's downstream flank are much weaker, a reflection of the absence at this time of any semblance of an EKE maximum along that flank. At all times the pattern of advective flux divergence primarily operates to shift the EKE distribution eastward, as would be expected given the large westerly component of the total flow.

The composite baroclinic conversion displays a wide variation with time. At $T - 24$ this term contributes a first-order positive EKE tendency over most of the cyclone's downstream flank, and a maximum in this tendency is collocated with the cyclone's primary EKE maximum (Fig. 6a). By $T - 12$, positive baroclinic conversion along the cyclone's downstream flank has intensified considerably (Fig. 6b). The maximum in conversion has shifted slightly to the north of the cyclone's primary EKE maximum, but remains in close proximity to it. During the 12 h between $T - 12$ and $T = 0$, a drastic decline in baroclinic conversion occurs along the cyclone's downstream flank (Fig. 6c). By $T = 0$, a positive conversion maximum remains collocated with this flank, but it is only of minimal first-order magnitude and has also shifted a notable distance downstream relative to the SLP minimum. At $T + 12$, a solitary, modest maximum in positive baroclinic conversion is evident well downstream from the surface cyclone, near the northernmost extent of significant EKE in the region.

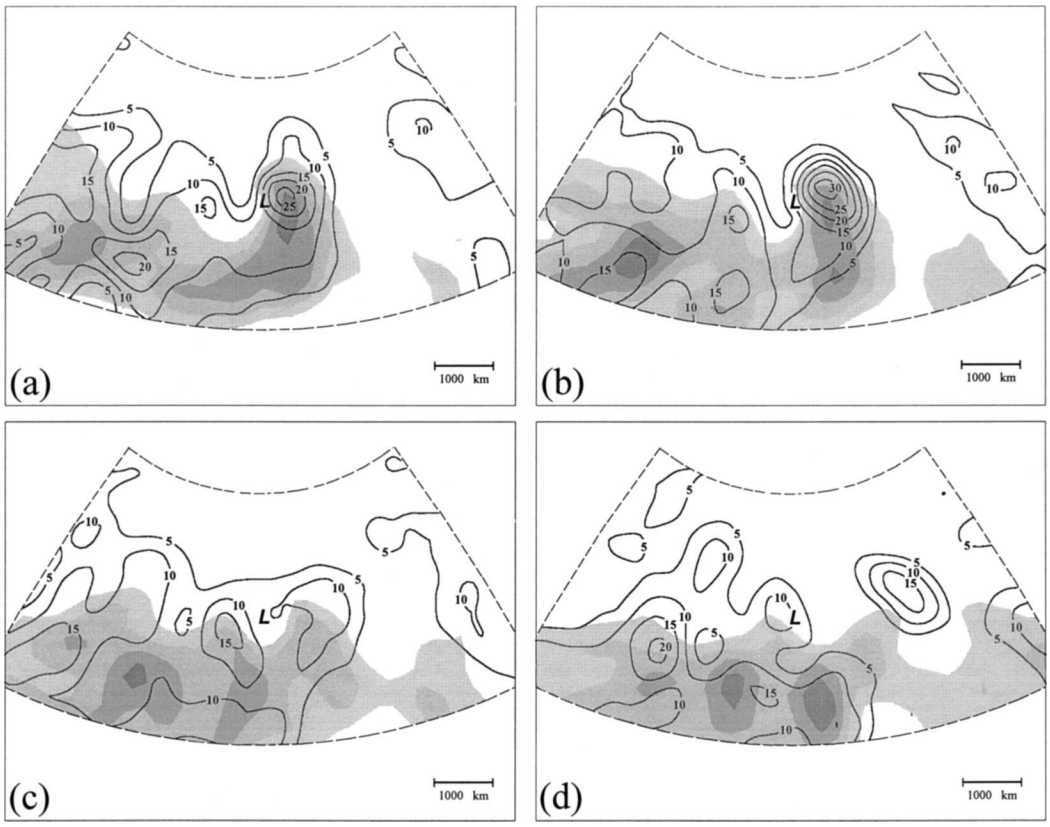

FIG. 6. (a) Gulf of Alaska region composite vertically averaged baroclinic conversion and EKE at time $T - 24$. Solid (short dashed) lines are positive (negative) values of baroclinic conversion labeled in 10^{-4} m^2 s^{-3} and contoured every 5×10^{-4} m^2 s^{-3} (-5×10^{-4} m^2 s^{-3}) beginning at 5×10^{-4} m^2 s^{-3} (-5×10^{-4} m^2 s^{-3}). EKE shaded as in Fig. 2. Bold L represents the position of the SLP minimum. Approximate length scale indicated in lower-right corner. Latitude and longitude are as in Fig. 2. (b) As in (a) but for time $T - 12$. (c) As in (a) but for time $T = 0$. (d) As in (a) but for time $T + 12$.

All other significant baroclinic conversion is confined to the south or west of the surface cyclone (Fig. 6d). Analysis of individual cases suggests that the solitary maximum of baroclinic conversion seen well to the east of the SLP minimum often coincides with the peak of the decaying cyclone's warm sector.

The meridional momentum correlation has a very consistent distribution during the composite analysis period (Fig. 7). The mechanism exerts a negative tendency that reaches first-order magnitude with respect to the primary EKE maximum. This negative tendency also encompasses a broad region that is persistently centered over the downstream flank of the cyclone. On the cyclone's upstream flank a broad but weaker positive tendency region is found. The negative EKE tendency associated with this term arises as follows. The primary EKE maximum is located along the downstream flank of the upper trough where the eddy meridional momentum (v) is positive. In addition, during the time period of the composite the cyclone and its primary EKE maximum evolve toward the end of the Pacific winter storm track (refer to Fig. 1a), where the mean eddy meridional momentum flux divergence ($\overline{\nabla_3 \cdot \upsilon \mathbf{v}'}$) is negative (i.e., there is a flux convergence). By definition, the storm track marks that region wherein the eddy components of the flow are, on average, relatively large. The implied diminishment (on average) of eddy activity as a flow exits the storm track might be expected to introduce a mean convergence of eddy momentum flux in the exit region. The mean eddy meridional momentum flux convergence is associated with a negative tendency in eddy meridional momentum. Thus, the positive eddy meridional momentum on the downstream flank of the upper trough experiences a negative tendency, which implies a decrease in magnitude of the eddy meridional momentum and a corresponding decrease in EKE.

The tendency contribution from the composite surface drag term is shown in Fig. 8 at each analysis time. At $T - 24$, the action of surface drag induces a broad, crescent-like maximum of negative tendency to the south of the SLP minimum (Fig. 8a). This tendency maximum is only of second-order magnitude. Tendencies of similar distribution and magnitude are associ-

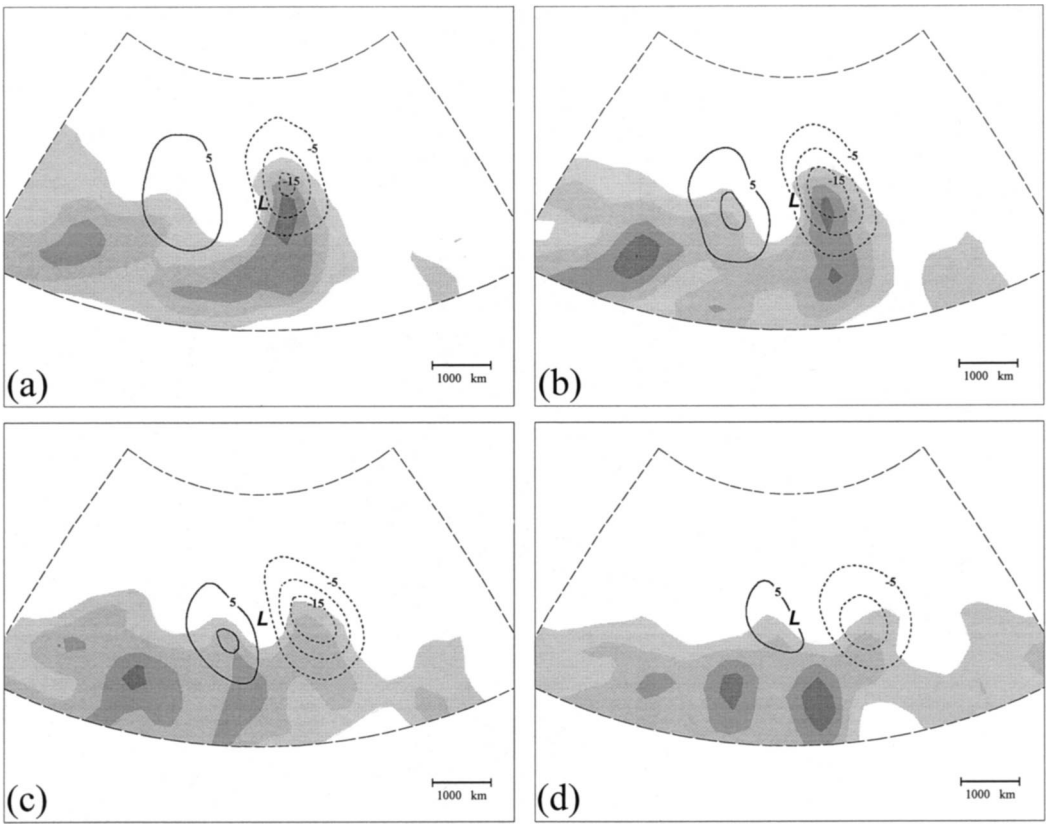

FIG. 7. (a) Gulf of Alaska region composite vertically averaged meridional momentum correlation and EKE at time $T - 24$. Solid (short dashed) lines are positive (negative) values of meridional momentum correlation labeled in 10^{-4} m^2 s^{-3} and contoured every 5×10^{-4} m^2 s^{-3} (-5×10^{-4} m^2 s^{-3}) beginning at 5×10^{-4} m^2 s^{-3} (-5×10^{-4} m^2 s^{-3}). EKE shaded as in Fig. 2. Bold L represents the position of the SLP minimum. Approximate length scale indicated in lower-right corner. Latitude and longitude are as in Fig. 2. (b) As in (a) but for time $T - 12$. (c) As in (a) but for time $T = 0$. (d) As in (a) but for time $T + 12$.

ated with surface drag at $T - 12$ and $T = 0$ (Figs. 8b,c). By $T + 12$, the action of surface drag no longer makes any noteworthy contributions to the EKE tendency in the vicinity of the SLP minimum or the downstream flank of the cyclone (Fig. 8d). It is interesting that the largest tendencies associated with surface drag occur on the southern flank of the cyclone since, for a cyclone making landfall in the Gulf of Alaska region, this flank would be situated away from the rugged coastal terrain. Apparently, in the cyclones of the Gulf of Alaska composite, the surface wind over the ocean is generally strong enough that it facilitates a greater energy loss through surface drag than does the interaction of the surface wind over land with the mountainous coastal terrain. It must be noted, though, that this result does not include the effect of surface drag associated with horizontal flux divergence of the rate of work by surface stress. Such an effect may be significant in the Gulf of Alaska region, where rapid transitions from ocean surface to extreme mountainous terrain are commonplace.

The composite residual term is presented at each of the analysis times together with the vertically averaged EKE in Fig. 9. At $T - 24$, the residuals throughout the composite grid contribute a predominantly negative tendency (Fig. 9a). With respect to the cyclone's primary EKE feature, the residuals are less than first order, except for those that form a negative maximum along the feature's northeastern flank. A similar residual distribution with respect to the primary EKE feature is found at $T - 12$ (Fig. 9b). Again, the residuals of first-order magnitude are limited to a negative maximum along the northeastern flank of the primary EKE feature. By $T = 0$, first-order residuals with respect to the primary EKE feature exist only as an isolated negative maximum on the feature's distant southeastern edge (Fig. 9c). Residuals with respect to the great majority of the EKE feature are of little significance. At $T + 12$ no significant residuals are found with respect to the modest EKE that remains along the cyclone's downstream flank (Fig. 9d).

Finally, terms of lesser importance with respect to the primary EKE feature are the zonal momentum correlation, shear generation, and curvature. These terms

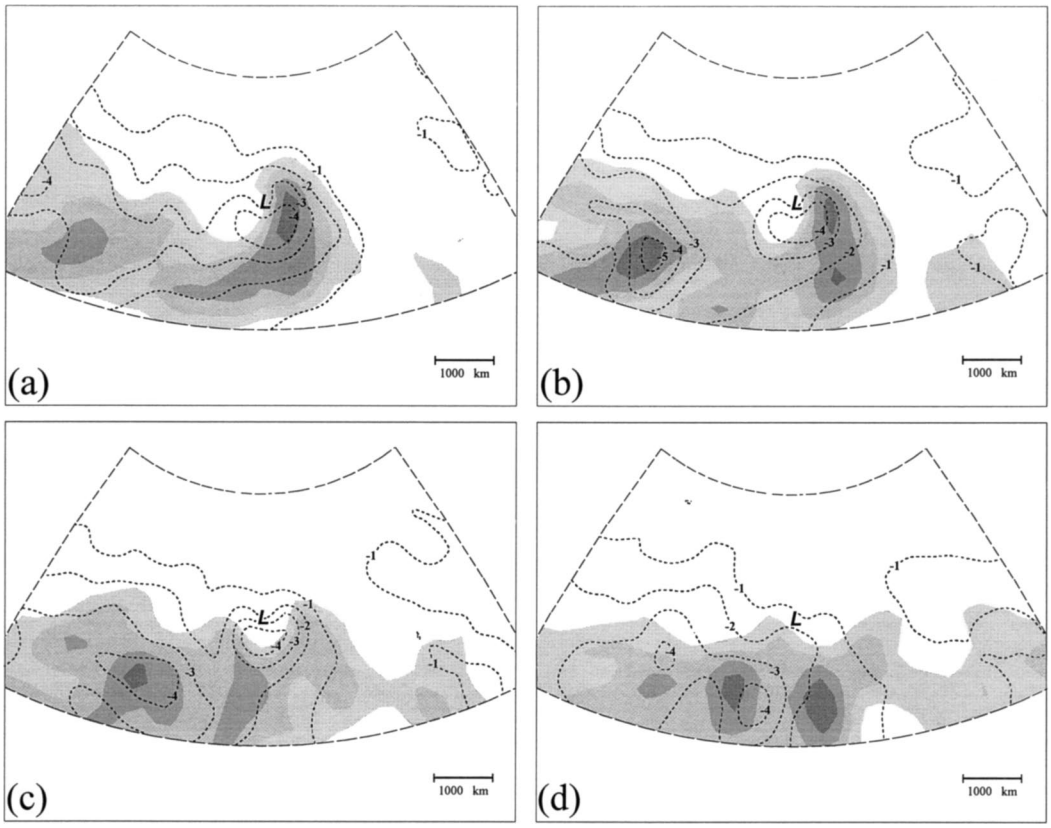

FIG. 8. (a) Gulf of Alaska region composite surface drag term and vertically averaged EKE at time $T - 24$. Solid (short dashed) lines are positive (negative) values of the surface drag term labeled in 10^{-4} m^2 s^{-3} and contoured every 1×10^{-4} m^2 s^{-3} (-1×10^{-4} m^2 s^{-3}) beginning at 1×10^{-4} m^2 s^{-3} (-1×10^{-4} m^2 s^{-3}). EKE shaded as in Fig. 2. Bold L represents the position of the SLP minimum. Approximate length scale indicated in lower-right corner. Latitude and longitude are as in Fig. 2. (b) As in (a) but for time $T - 12$. (c) As in (a) but for time $T = 0$. (d) As in (a) but for time $T + 12$.

consistently produce EKE tendencies with respect to the cyclone's downstream flank of second-order magnitude or less, and so are not detailed here. It is interesting to note, however, that the negatively tilted primary trough and its associated primary EKE feature are consistently influenced by *negative* values of the shear generation term. This circumstance arises because of the positioning of the trough north of the mean jet core, and demonstrates why one should be mindful that not all negatively tilted troughs amplify through barotropic energy growth.

Some additional observations follow about the most significant EKE tendency terms. The residual term attains a first-order magnitude, but only in a limited region that is displaced from that part of the EKE distribution that experiences the most marked decline during the analysis period. Furthermore, the residuals in this limited region do not at any time have dominant first-order values. These circumstances indicate that the first-order residuals that appear in the analysis are not particularly significant. It is also important to note that the residuals at each analysis time are of predominantly negative sign. This suggests that the residuals do not, on the whole, reflect computational errors but rather reflect the action of the internal dissipation, surface drag, and gravity wave drag terms, which are not represented in the EKE tendency equation. These observations, and the fact that the residuals are, in large part, relatively small, indicate that the energy budget given by the tendency terms is fundamentally reliable.

The positive tendencies associated with the advective flux divergence term are found to attain the largest absolute values of any term, a result consistent with the findings of Chang (2000). These tendencies support a general northward and eastward progression (relative to the cyclone's upper trough or sea level pressure minimum) of the EKE feature on the cyclone's downstream flank. Some propagation of this EKE feature in relation to the sea level pressure minimum does occur during the analysis period (refer to Fig. 2). Notably, however, the EKE feature remains collocated with the downstream flank of the cyclone's upper trough throughout the period. Thus, despite its large values, the advective flux divergence does not effectively dissociate the EKE

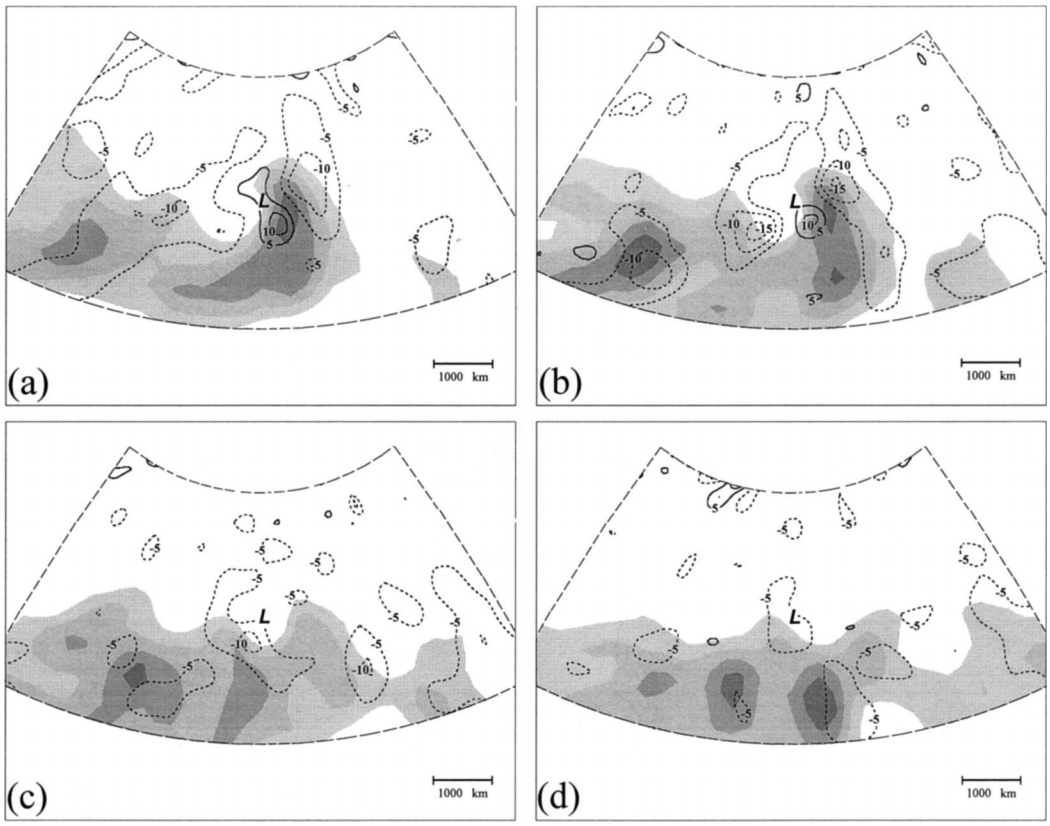

FIG. 9. (a) Gulf of Alaska region composite residual term and vertically averaged EKE at time $T - 24$. Solid (short dashed) lines are positive (negative) values of the residual term labeled in 10^{-4} m^2 s^{-3} and contoured every 5×10^{-4} m^2 s^{-3} (-5×10^{-4} m^2 s^{-3}) beginning at 5×10^{-4} m^2 s^{-3} (-5×10^{-4} m^2 s^{-3}). EKE shaded as in Fig. 2. Bold L represents the position of the SLP minimum. Approximate length scale indicated in lower-right corner. Latitude and longitude are as in Fig. 2. (b) As in (a) but for time $T - 12$. (c) As in (a) but for time $T = 0$. (d) As in (a) but for time $T + 12$.

feature from the cyclone's downstream flank, and so is not considered a determining factor in the composite EKE budget.

With regard only to negative tendency values, the radiative flux divergence term is found to impart the largest tendency with respect to the EKE feature on the cyclone's downstream flank. The meridional momentum correlation also imparts a significant negative tendency, but at the critical times $T - 12$ and $T = 0$ the maximum value of this tendency is substantially less than the maximum value of the radiative dispersion. More specifically, the maximum value of the meridional momentum correlation is only approximately 60% (50%) of that of the radiative dispersion at $T - 12$ ($T = 0$). The negative tendency associated with the surface drag term, meanwhile, is consistently only of second-order magnitude and is considerably less important than the tendency associated with either the radiative dispersion or the meridional momentum correlation. It is noted that calculation of the surface drag term neglected contributions from the horizontal flux divergence of the rate of work by surface stress. Also, substantial approximation is entailed in the parameterization of surface stress associated with complex terrain in a global numerical weather prediction model of relatively low resolution. An assessment of the impact of surface drag should include some allowance for the potential errors introduced in association with these realities. One means of doing so is to consider the residual to be dominated by unaccounted surface drag effects. This may be a reasonable assumption for two reasons. First, the residual is predominantly negative. Second, at $T - 24$ and $T - 12$ some of the largest residual values are found in the northeastern and eastern quadrants of the cyclone. For an intense landfalling cyclone in the Gulf of Alaska, these are two quadrants wherein the cyclone's surface winds would be strongly interacting with rugged terrain, and wherein one might intuitively expect significant surface drag effects. These two quadrants also happen to be ones wherein the computed values of the surface drag term are not significant (refer to Fig. 8). Assuming that the residual is dominated by unaccounted surface drag effects, the sum of the surface drag term and the residual can be interpreted as an estimate of the ''true'' impact

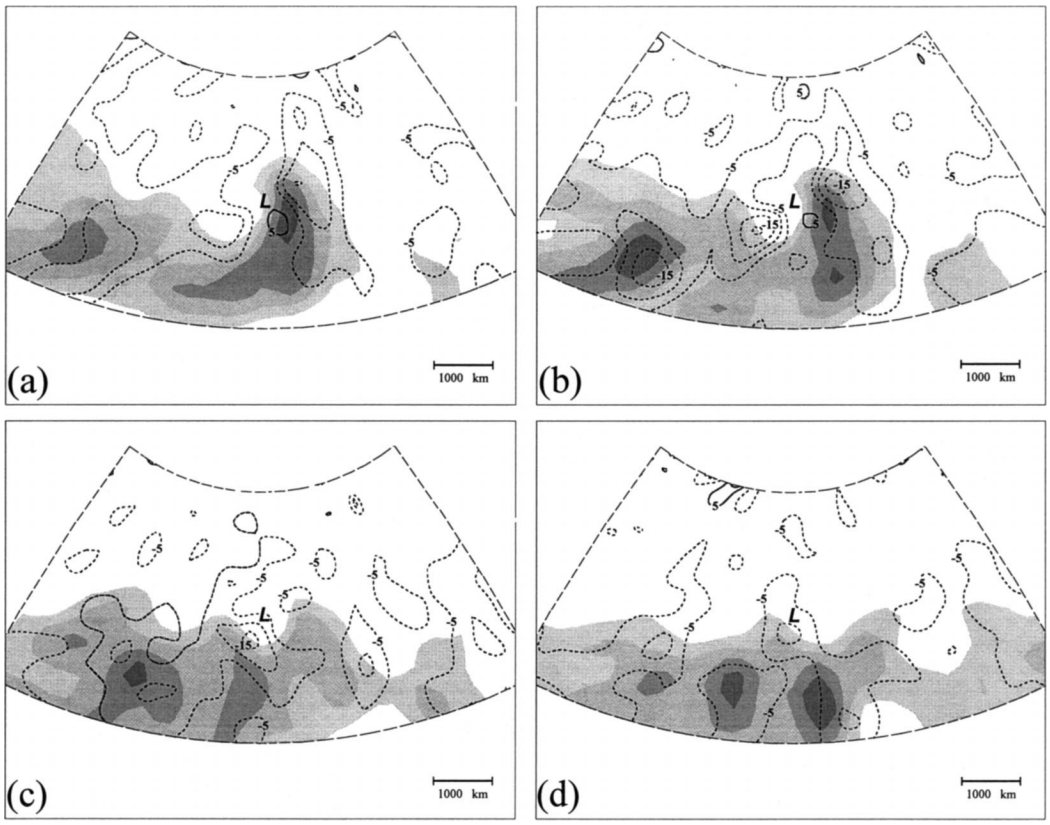

FIG. 10. (a) The sum of the Gulf of Alaska region composite surface drag term and residual, together with the composite vertically averaged EKE, at time $T - 24$. Solid (short dashed) lines are positive (negative) values of the sum labeled in 10^{-4} m^2 s^{-3} and contoured every 5×10^{-4} m^2 s^{-3} (-5×10^{-4} m^2 s^{-3}) beginning at 5×10^{-4} m^2 s^{-3} (-5×10^{-4} m^2 s^{-3}). EKE shaded as in Fig. 2. Bold L represents the position of the SLP minimum. Approximate length scale indicated in lower-right corner. Latitude and longitude are as in Fig. 2. (b) As in (a) but for time $T - 12$. (c) As in (a) but for time $T = 0$. (d) As in (a) but for time $T + 12$.

of surface drag. Assessment of this sum shows that the true EKE tendency induced by surface drag would at most only amount to roughly 50% of the value of the radiative dispersion (Fig. 10).

5. Bering Sea region composite local energetics diagnostics

a. Vertically averaged EKE evolution

The Bering Sea region composite 300-hPa geopotential height and vertically averaged EKE for each analysis time are displayed in Fig. 11. At $T - 24$, the composite cyclone is associated with a well-developed trough and ridge in the 300-hPa geopotential height (Fig. 11a). Downstream of the primary trough and ridge is a trough of lesser amplitude. This downstream trough occupies the entire meridional extent of the composite domain, and exhibits its greatest amplitude in the southeast corner of the domain. A crescent-shaped EKE feature on the downstream flank of the primary trough dominates the EKE distribution at $T - 24$. This feature displays a meridionally elongated maximum, located immediately to the southeast of the SLP minimum. Downstream of the primary EKE feature and along the downstream flank of the primary ridge is a band of EKE of modest magnitude. A broad relative maximum is found at the southern end of this band, and a much smaller relative maximum is found at the band's northern end.

At $T - 12$ the height contours of the primary trough and ridge are more amplified in the vicinity of the SLP minimum, suggesting that a closed upper low is forming there (Fig. 11b). Also, the downstream trough has slightly amplified. The primary EKE maximum is of the same intensity as before but is displaced slightly eastward relative to the SLP minimum. Meanwhile, the portion of the primary EKE feature that wraps around the SLP minimum has diminished in intensity along the north side of this minimum. Downstream of the primary trough, a second sizeable EKE maximum has taken shape along the downstream flank of the primary ridge.

At $T = 0$, the primary trough and ridge both remain very well developed, and a closed low is present within the primary trough, centered almost directly over the SLP minimum (Fig. 11c). The primary EKE maximum

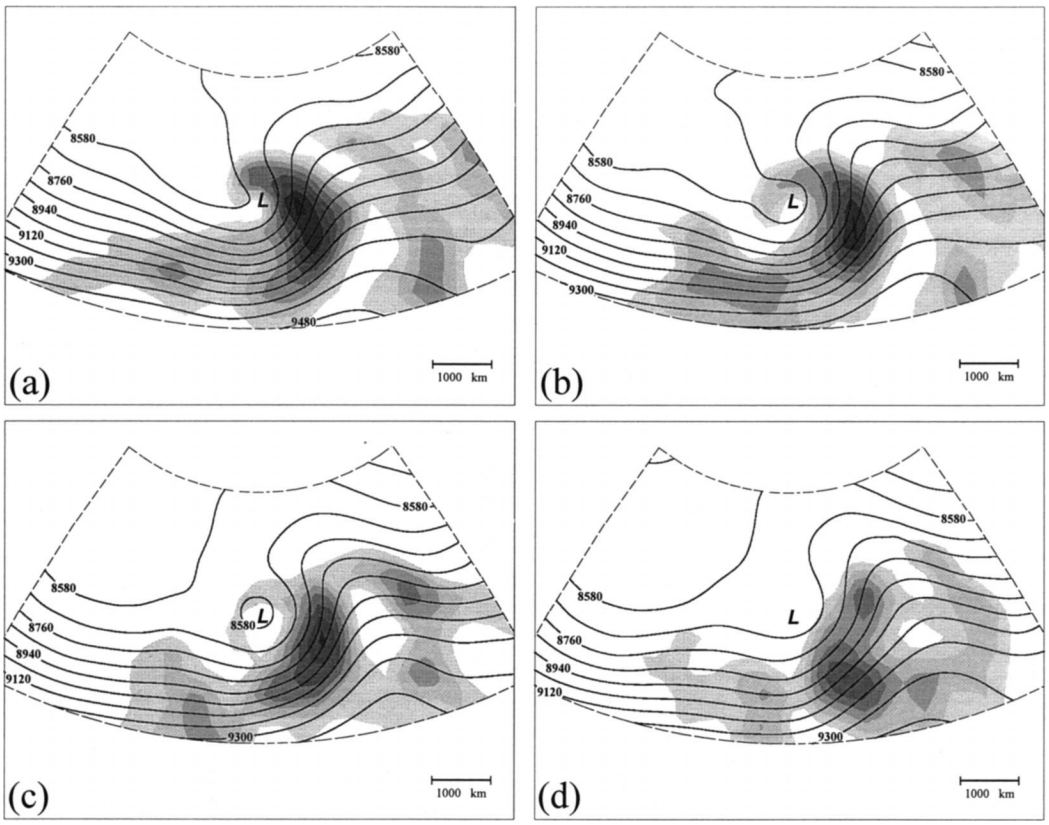

FIG. 11. (a) Bering Sea region composite vertically averaged EKE and 300-hPa geopotential height at $T - 24$. EKE is shaded every 30 $m^2\ s^{-2}$ beginning at 150 $m^2\ s^{-2}$. Geopotential height is labeled in dam and contoured every 9 dam. Bold L represents the position of the SLP minimum. Approximate length scale indicated in lower-right corner. Latitude and longitude are as in Fig. 2. (b) As in (a) but for time $T - 12$. (c) As in (a) but for time $T = 0$. (d) As in (a) but for time $T + 12$.

is still quite prominent and attains a similar magnitude as before. However, the very highest EKE values are now restricted to a smaller area, and the EKE maximum has also been displaced farther eastward relative to the SLP minimum. Additionally, a significant decline has occurred in the EKE to the north of the SLP minimum. Elsewhere, the downstream trough has amplified considerably, and the northernmost EKE maximum on the downstream flank of the primary ridge is more intense.

At $T + 12$, a closed low is no longer present within the primary trough and the curvature of this trough's height contours has decreased, but the amplitudes of the primary trough and ridge have not changed substantially (Fig. 11d). Furthermore, the geopotential height contours suggest the continued presence of a prominent downstream trough. The primary trough is now associated with two notable EKE maxima, one maximum being located near its base and the other on its downstream flank. While the EKE on the downstream flank of the primary trough has generally diminished, the EKE maximum that remains there is still fairly intense, and the maximum near the base of the trough is very intense. Downstream of the primary trough, the two EKE maxima on the downstream flank of the primary ridge have disappeared, leaving a meridionally oriented band of EKE of modest magnitude.

b. *Vertically averaged local energetics tendency terms*

The roles of the local energetics tendency terms and their hierarchy in this composite are found to be very similar to those in the Gulf of Alaska composite. Thus, only the action of the two most important terms, the radiative flux divergence and baroclinic conversion terms, is described here.

The vertically averaged AGF vectors, radiative flux divergence term, and EKE are plotted in Fig. 12 (Fig. 13) at times $T - 24$ and $T - 12$ ($T = 0$ and $T + 12$). At $T - 24$ a vortex of intense AGF is centered close to the SLP minimum (Fig. 12a). Downstream AGF from the eastern flank of the primary EKE feature is pronounced, and upstream (westward) AGF emanating from the northern flank of the AGF vortex is also notable. Significant radiative flux divergence is occurring over the northern edge of the primary EKE feature and over that portion of this feature that wraps around the north side of the SLP minimum. Radiative flux diver-

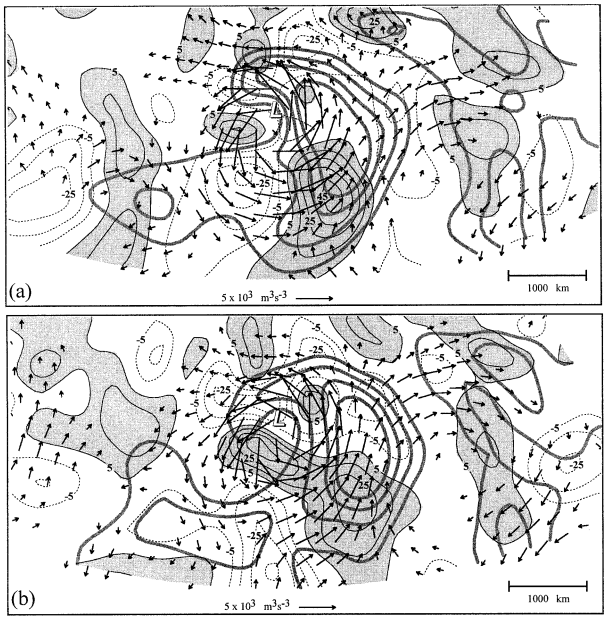

FIG. 12. (a) Bering Sea region composite vertically averaged AGF vectors, radiative flux divergence term ($-\nabla_3 \cdot \mathbf{V}'\phi'$), and EKE at time $T - 24$. AGF vectors are solid arrows in units of $m^3\,s^{-3}$ with reference arrow indicated. Thin solid (dashed) lines are positive (negative) values of the radiative flux divergence term labeled in 10^{-4} $m^2\,s^{-3}$ and contoured every 1×10^{-3} $m^2\,s^{-3}$ (-1×10^{-3} $m^2\,s^{-3}$) beginning at 5×10^{-4} $m^2\,s^{-3}$ (-5×10^{-4} $m^2\,s^{-3}$). Positive values of the radiative flux divergence term are shaded. Thick gray solid lines are vertically averaged EKE contoured every 40 $m^2\,s^2$ between 170 and 290 $m^2\,s^2$. Outlined L represents the position of the SLP minimum. Approximate length scale indicated in lower-right corner. (b) As in (a) but for time $T - 12$.

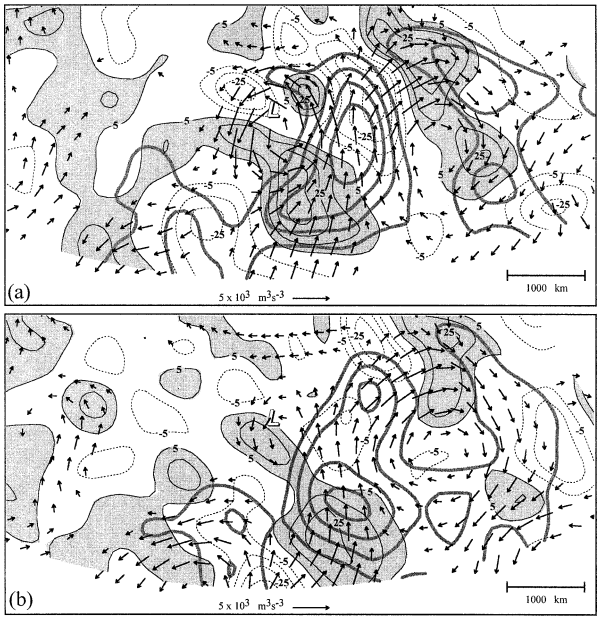

FIG. 13. (a) As in Fig. 12a, but for time $T = 0$. (b) As in (a) but for time $T + 12$.

gence of lesser magnitude is occurring along the primary EKE feature's eastern flank. Flux convergence is very strong at the southern end of the primary EKE feature, a result of convergence within the AGF vortex and also of the merger with this vortex of AGF entering the southern portion of the composite domain. A smaller region of significant flux convergence is found to the immediate southwest of the SLP minimum, and others exist at or near the northwestern edge of the primary EKE feature. Additionally, the downstream AGF that emanates from the primary EKE feature experiences significant convergence within the eastern part of the composite domain.

At $T - 12$, the overall pattern of the AGF vectors and the radiative flux divergence term is very similar. The AGF vortex centered near the SLP minimum and the downstream AGF from the primary EKE feature both remain prominent, and upstream AGF is still occurring, emanating from the northern and western flank of the AGF vortex (Fig. 12b). Much of the northern portion of the primary EKE feature is influenced by significant radiative flux divergence. The divergence has increased in magnitude over that portion of the primary EKE feature that wraps around to the north and west of the SLP minimum. Meanwhile, an intense radiative flux convergence maximum persists at the southern end of the primary EKE feature, and flux convergence has increased in magnitude and spatial extent to the immediate southwest and south of the SLP minimum.

By $T = 0$, downstream AGF from the primary EKE feature has become very intense (Fig. 13a). A notable increase in radiative flux convergence downstream of the primary EKE feature has accompanied the intensification of downstream AGF. Also, radiative flux divergence has increased over much of the northern portion of the primary EKE feature, particularly along the feature's northeastern edge. Significant AGF into the southern part of the primary EKE maximum continues, and this again contributes to strong flux convergence in that area. Also, an AGF vortex remains centered near the SLP minimum, though the AGF vectors that comprise the vortex have generally experienced a reduction in magnitude.

At $T + 12$, significant AGF continues to occur along the entire downstream flank of the cyclone, and extensive downstream AGF emanates from the EKE maximum located to the northeast of the SLP minimum (Fig. 13b). Radiative flux divergence is locally very intense near this maximum, and is generally present over much of the cyclone's downstream flank. In contrast, strong radiative flux convergence operates over most of the prominent EKE maximum located to the southeast of the SLP minimum. This convergence occurs in association with significant AGF that largely originates from points well south of the decaying cyclone. Elsewhere, a very weak AGF vortex is still evident near the SLP minimum.

The composite vertically averaged baroclinic con-

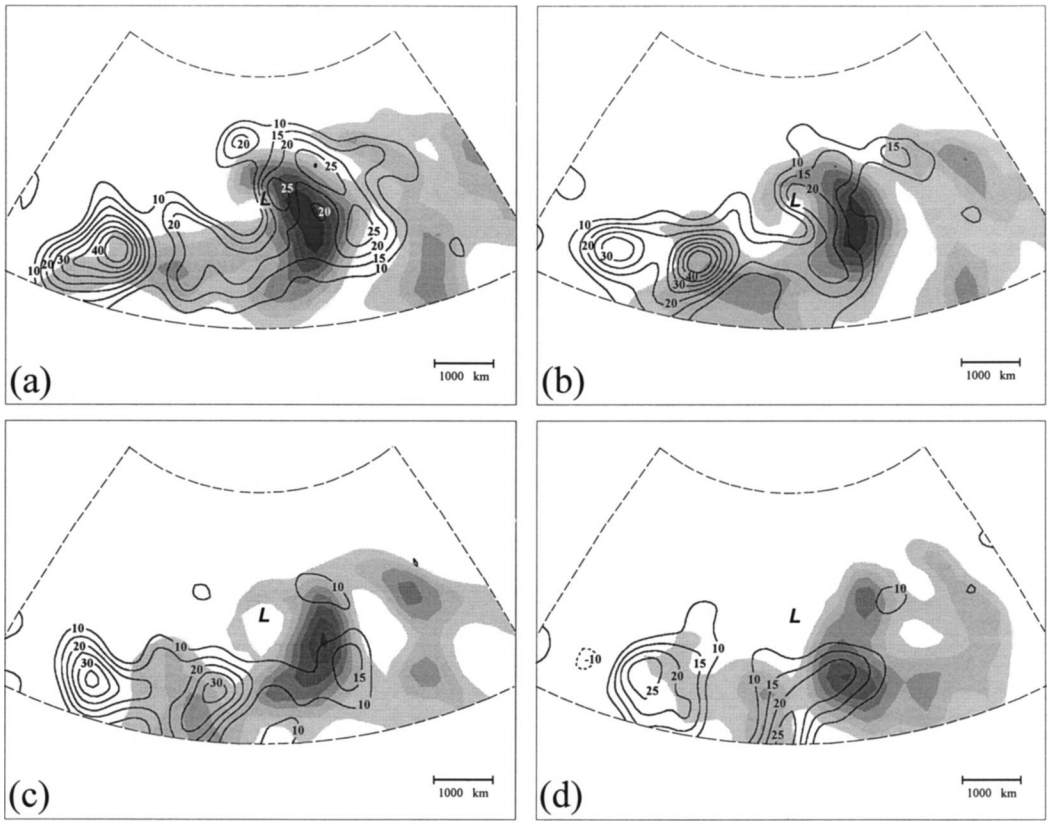

FIG. 14. (a) Bering Sea region composite vertically averaged baroclinic conversion and EKE at time $T - 24$. Solid (short dashed) lines are positive (negative) values of baroclinic conversion labeled in 10^{-4} m^2 s^{-3} and contoured every 5×10^{-4} m^2 s^{-3} (-5×10^{-4} m^2 s^{-3}) beginning at 1×10^{-3} m^2 s^{-3} (-1×10^{-3} m^2 s^{-3}). EKE shaded as in Fig. 11. Bold L represents the position of the SLP minimum. Approximate length scale indicated in lower-right corner. Latitude and longitude are as in Fig. 2. (b) As in (a) but for time $T - 12$. (c) As in (a) but for time $T = 0$. (d) As in (a) but for time $T + 12$.

version and EKE are shown in Fig. 14 at each analysis time. At $T - 24$ significant positive baroclinic conversion is occurring throughout the vicinity of the crescent-shaped primary EKE feature (Fig. 14a). Three relative maxima in baroclinic conversion are arranged in an arc along the northern and eastern flanks of this feature, while another maximum is located immediately east of the SLP minimum. Two other significant positive baroclinic conversion maxima are present upstream of the primary EKE feature, the one farthest upstream being very intense. The northernmost portion of the band of EKE downstream of the primary EKE feature is also influenced by fairly significant positive baroclinic conversion. Elsewhere downstream of the primary EKE feature the baroclinic conversion is much less significant.

By $T - 12$, the positive baroclinic conversion maxima that formed an arc along the northern and eastern flanks of the primary EKE feature have disappeared (Fig. 14b). A single conversion maximum of reduced magnitude is now observed in the vicinity of this feature, extending from the SLP minimum southeastward to the feature's southern end. Positive baroclinic conversion continues to be very intense upstream of the primary EKE feature.

By $T = 0$, positive baroclinic conversion in the vicinity of the cyclone has in general decreased significantly (Fig. 14c). Minimal baroclinic conversion is occurring in the vicinity of the SLP minimum, and the primary EKE feature is influenced by only two modest conversion maxima arrayed along its northern and eastern edges. By $T + 12$, significant baroclinic conversion is only occurring upstream of the SLP minimum (Fig. 14d).

6. Discussion and conclusions

Two regional local energetics composites of tropospheric-deep cyclone decay were constructed based upon 49 cyclones in the Gulf of Alaska region and 18 cyclones in the Bering Sea region whose decay was marked by rapid surface cyclolysis. Most of the defining characteristics of the two composites are similar. One such characteristic common to both composites is the secondary role of surface drag throughout the decay period. Indeed, the action of surface drag remains secondary even when a generous accounting is made for uncertainty in the surface drag calculation. The subor-

dinate role of surface drag in the Gulf of Alaska composite is particularly interesting, given that the cyclones in this composite decay in close proximity to rugged and extensive high-elevation terrain. This circumstance suggests that surface drag associated with mountainous terrain is not often the principal energetic decay mechanism in a cyclolysis event.

A second important and common characteristic of the two composites is the preeminence of radiative dispersion as a sink of EKE. Since the radiative dispersion is maximized in the upper troposphere, it logically follows that cyclone decay marked by rapid surface cyclolysis is driven from the upper troposphere, not from the surface. Another notable characteristic of both composites is the occurrence of organized and extensive downstream AGF from the decaying cyclone's primary EKE feature. Prominent downstream AGF and preeminent radiative dispersion are two fundamental characteristics of the downstream development model of cyclone decay, and carry with them significant implications. First, the role of radiative dispersion as the principal sink of EKE implies that a substantial fraction of the EKE originally associated with the primary cyclone remains in the flow as the cyclone decays. Second, the highly uniform and far-reaching downstream AGF implies that the EKE dispersed from the decaying cyclone may ultimately be important in subsequent development in regions distant from the cyclone. These implications are especially interesting given that 1) cyclone decay marked by rapid surface cyclolysis tends to occur toward the end of the Pacific winter storm track, a region that is by definition a terminus of eddy activity, and 2) this decay often occurs in proximity to extensive and high-elevation terrain, terrain that might reasonably be considered as very disruptive of any continued significant propagation of eddy energy.

An additional noteworthy characteristic common to the two composites is the occurrence of a pronounced decline in baroclinic conversion during the analysis period. A decline in baroclinic conversion is certainly not unexpected. Rather, it is consistent with the notion that baroclinic growth typically declines by the time a cyclone approaches or enters the occluded or decay phases of its life cycle. What may be exceptional is the abruptness and extent of the curtailment in baroclinic conversion. Indeed, the fractional decline in baroclinic conversion observed between $T - 12$ and $T = 0$ in the Gulf of Alaska composite is considerably greater than most fractional declines observed in association with the many troughs studied by Chang (2000; refer to his Figs. 9, 10, and 12). Most important, the occurrence of this dramatic curtailment just as the radiative dispersion and other EKE sinks attain their peak intensity is likely what enables the marked decline in EKE on the cyclone's downstream flank to occur. In short, the rapid and pronounced decline in baroclinic conversion, the cyclone's dominant EKE source, makes the simultaneous and intense action of radiative dispersion and the lesser action of other EKE sinks very efficient at reducing the magnitude of the EKE on the cyclone's downstream flank. Further investigation may reveal specific reasons for the timing and extent of the curtailment of baroclinic conversion in these cyclones.

While the two composites share the above key aspects, they also exhibit some intriguing contrasts as well. One of these contrasts involves the occurrence of prominent downstream development. In the Bering Sea composite a prominent EKE maximum develops on the downstream flank of the primary ridge between $T - 24$ and $T = 0$, and the downstream trough amplifies throughout the analysis period. These circumstances are indicative of considerable downstream development. Meanwhile, in the Gulf of Alaska composite a modest EKE maximum is found downstream of the cyclone at each analysis time, and this maximum experiences a small amount of intensification between $T - 12$ and $T = 0$. However, at no point does this maximum approach the original intensity of the decaying cyclone. Thus, despite the substantial downstream dispersion from the decaying cyclone's primary EKE feature in the Gulf of Alaska composite, significant development does not occur immediately downstream.

The lack of intense downstream development in the vicinity of the decaying cyclone in the Gulf of Alaska composite is consistent with the absence of significant convergence in the downstream AGF. A sufficient explanation for why the downstream AGF in the Gulf of Alaska composite is less convergent than that in the Bering Sea composite is not forthcoming from the diagnostics. However, the relative lack of AGF convergence, and the extension of organized AGF to the southern boundary of the composite domain, indicate that cyclone decay associated with rapid surface cyclolysis in the Gulf of Alaska region involves considerable dispersal of EKE to points downstream but well south of the decay location. This might have important implications for development in the vicinity of the western United States and, hence, suggests that further investigation of the impact of decay events in the Gulf of Alaska region on forecasts of development over the western United States could be revealing.

Another notable contrast between the two composites is in the extent of the decline of vertically averaged EKE in the decaying cyclone's vicinity. In the Gulf of Alaska composite the EKE in the vicinity of the cyclone is greatly diminished by the end of the analysis period, while in the Bering Sea composite the EKE at many locations along the primary trough remains significant at time $T + 12$. Most unusual is the continued significance of the EKE on the trough's downstream flank in the Bering Sea composite. The persistence of relatively high EKE on this flank likely can be attributed to the consistent and strong convergence of AGF at the southern end of the primary EKE feature during the analysis period. The AGF convergence deposits considerable EKE at that location, and this EKE is then advected in

the downstream direction, replenishing some of that which is lost to radiative flux divergence along the downstream flank of the primary trough. It is notable that strong radiative flux convergence at the southern end of the primary EKE feature, and the corresponding replenishing effect, are absent in the Gulf of Alaska composite. An obvious question, then, is why a prominent source of AGF is typically convenient to the decaying cyclones in the Bering Sea composite but not to those in the Gulf of Alaska composite. This circumstance may imply that the Bering Sea events tend to take place in association with vigorous wave trains and that the Gulf of Alaska events tend to occur in isolation. Further investigation is needed to effectively address questions such as this.

Acknowledgments. This research was supported by the National Science Foundation under Grant ATM-9733127. We gratefully acknowledge the ECMWF and NCAR for the use of the ECMWF reanalysis data, and Unidata for their support of GEMPAK. The comments of two anonymous reviewers helped improve this manuscript.

APPENDIX A

Derivation of the EKE Time-Tendency Equation

The derivation begins with the following forms of the frictionless horizontal momentum equations in spherical, isobaric coordinates:

$$\frac{\partial u}{\partial t} = -\mathbf{V}\cdot\nabla_3 u - \frac{1}{r\cos\psi}\frac{\partial \phi}{\partial \lambda} + fv + \frac{uv}{r}\tan\psi \quad \text{(A1)}$$

$$\frac{\partial v}{\partial t} = -\mathbf{V}\cdot\nabla_3 v - \frac{1}{r}\frac{\partial \phi}{\partial \psi} - fu - \frac{u^2}{r}\tan\psi. \quad \text{(A2)}$$

Here $\mathbf{V} = u\hat{\imath} + v\hat{\jmath} + \omega\hat{k}$. A partitioning of u, v, and ϕ into time-mean and instantaneous components transforms Eq. (A1) and (A2) into, respectively,

$$\frac{\partial \overline{u}}{\partial t} + \frac{\partial u'}{\partial t} = -\overline{\mathbf{V}}\cdot\nabla_3\overline{u} - \overline{\mathbf{V}}\cdot\nabla_3 u' - \mathbf{V}'\cdot\nabla_3\overline{u} - \mathbf{V}'\cdot\nabla_3 u' - \frac{1}{r\cos\psi}\left(\frac{\partial\overline{\phi}}{\partial\lambda} + \frac{\partial\phi'}{\partial\lambda}\right) + f\overline{v} + fv' + \frac{\tan\psi}{r}(\overline{u}\,\overline{v} + \overline{u}v' + u'\overline{v} + u'v') \quad \text{(A3)}$$

$$\frac{\partial \overline{v}}{\partial t} + \frac{\partial v'}{\partial t} = -\overline{\mathbf{V}}\cdot\nabla_3\overline{v} - \overline{\mathbf{V}}\cdot\nabla_3 v' - \mathbf{V}'\cdot\nabla_3\overline{v} - \mathbf{V}'\cdot\nabla_3 v' - \frac{1}{r}\left(\frac{\partial\overline{\phi}}{\partial\psi} + \frac{\partial\phi'}{\partial\psi}\right) - f\overline{u} - fu' - \frac{\tan\psi}{r}(\overline{u}\,\overline{u} + 2u'\overline{u} + u'u'). \quad \text{(A4)}$$

Time averaging Eq. (A3) and (A4) yields the equations for $\partial\overline{u}/\partial t$ and $\partial\overline{v}/\partial t$.

$$\frac{\partial \overline{u}}{\partial t} = -\overline{\mathbf{V}}\cdot\nabla_3\overline{u} - \overline{\mathbf{V}'\cdot\nabla_3 u'} - \frac{1}{r\cos\psi}\left(\frac{\partial\overline{\phi}}{\partial\lambda}\right) + f\overline{v} + \frac{\tan\psi}{r}[\overline{u}\,\overline{v} + \overline{u'v'}] \quad \text{(A5)}$$

$$\frac{\partial \overline{v}}{\partial t} = -\overline{\mathbf{V}}\cdot\nabla_3\overline{v} - \overline{\mathbf{V}'\cdot\nabla_3 v'} - \frac{1}{r}\left(\frac{\partial\overline{\phi}}{\partial\psi}\right) - f\overline{u} - \frac{\tan\psi}{r}(\overline{u}\,\overline{u} + \overline{u'u'}). \quad \text{(A6)}$$

Subtraction of (A5) from (A3) [(A6) from (A4)] yields the equation for $\partial u'/\partial t$ ($\partial v'/\partial t$):

$$\frac{\partial u'}{\partial t} = -\overline{\mathbf{V}}\cdot\nabla_3 u' - \mathbf{V}'\cdot\nabla_3\overline{u} - \mathbf{V}'\cdot\nabla_3 u' - \overline{\mathbf{V}'\cdot\nabla_3 u'} - \frac{1}{r\cos\psi}\left(\frac{\partial\phi'}{\partial\lambda}\right) + fv' + \frac{\tan\psi}{r}(\overline{u}v' + u'\overline{v} + u'v' - \overline{u'v'}) \quad \text{(A7)}$$

$$\frac{\partial v'}{\partial t} = -\overline{\mathbf{V}}\cdot\nabla_3 v' - \mathbf{V}'\cdot\nabla_3\overline{v} - \mathbf{V}'\cdot\nabla_3 v' - \overline{\mathbf{V}'\cdot\nabla_3 v'} - \frac{1}{r}\left(\frac{\partial\phi'}{\partial\psi}\right) - fu' - \frac{\tan\psi}{r}(2u'\overline{u} + u'u' - \overline{u'u'}). \quad \text{(A8)}$$

The continuity equations $\nabla_3\cdot\overline{\mathbf{V}} = 0$ and $\nabla_3\cdot\mathbf{V}' = 0$ allow the terms $u'(\nabla_3\cdot\overline{\mathbf{V}})$, $u'(\nabla_3\cdot\mathbf{V}')$, and $u'(\nabla_3\cdot\mathbf{V}')$ [$v'(\nabla_3\cdot\overline{\mathbf{V}})$, $v'(\nabla_3\cdot\mathbf{V}')$, and $v'(\nabla_3\cdot\mathbf{V}')$] to be subtracted from (A7) [(A8)]:

$$\frac{\partial u'}{\partial t} = -[\overline{\mathbf{V}}\cdot\nabla_3 u' + u'(\nabla_3\cdot\overline{\mathbf{V}})] - \mathbf{V}'\cdot\nabla_3\overline{u} - [\mathbf{V}'\cdot\nabla_3 u' + u'(\nabla_3\cdot\mathbf{V}')] - [\overline{\mathbf{V}'\cdot\nabla_3 u'} + \overline{u'(\nabla_3\cdot\mathbf{V}')}] - \frac{1}{r\cos\psi}\left(\frac{\partial\phi'}{\partial\lambda}\right) + fv' + \frac{\tan\psi}{r}(\overline{u}v' + u'\overline{v} + u'v' - \overline{u'v'}) \quad \text{(A9)}$$

$$\frac{\partial v'}{\partial t} = -[\overline{\mathbf{V}} \cdot \nabla_3 v' + v'(\nabla_3 \cdot \overline{\mathbf{V}})] - \mathbf{V}' \cdot \nabla_3 \overline{v} - [\mathbf{V}' \cdot \nabla_3 v' + v'(\nabla_3 \cdot \mathbf{V}')] - [\overline{\mathbf{V}' \cdot \nabla_3 v'} + \overline{v'(\nabla_3 \cdot \mathbf{V}')}]$$
$$- \frac{1}{r}\left(\frac{\partial \phi'}{\partial \psi}\right) - fu' - \frac{\tan\psi}{r}(2u'\overline{u} + u'u' - \overline{u'u'}). \quad \text{(A10)}$$

The two terms within each of the large brackets in (A9) and (A10) can be combined into a single term of flux form. Thus, (A9) and (A10) become

$$\frac{\partial u'}{\partial t} = -\nabla_3 \cdot \overline{\mathbf{V}} u' - \mathbf{V}' \cdot \nabla_3 \overline{u} - \nabla_3 \cdot \mathbf{V}' u' - \overline{\nabla_3 \cdot \mathbf{V}' u'}$$
$$- \frac{1}{r \cos\psi}\left(\frac{\partial \phi'}{\partial \lambda}\right) + fv'$$
$$+ \frac{\tan\psi}{r}(\overline{u} v' + u'\overline{v} + u'v' - \overline{u'v'}) \quad \text{(A11)}$$

$$\frac{\partial v'}{\partial t} = -\nabla_3 \cdot \overline{\mathbf{V}} v' - \mathbf{V}' \cdot \nabla_3 \overline{v} - \nabla_3 \cdot \mathbf{V}' v' - \overline{\nabla_3 \cdot \mathbf{V}' v'}$$
$$- \frac{1}{r}\left(\frac{\partial \phi'}{\partial \psi}\right) - fu' - \frac{\tan\psi}{r}(2u'\overline{u} + u'u' - \overline{u'u'}). \quad \text{(A12)}$$

Combining the first and third terms on the right-hand side of both (A11) and (A12), and multiplying (A11) by u' and (A12) by v' produces

$$\frac{\partial}{\partial t}\left(\frac{1}{2}u'^2\right) = -\nabla_3 \cdot \mathbf{V}\frac{1}{2}u'^2 - u'\mathbf{V}' \cdot \nabla_3 \overline{u} - u'\overline{\nabla_3 \cdot \mathbf{V}' u'}$$
$$- \frac{u'}{r \cos\psi}\left(\frac{\partial \phi'}{\partial \lambda}\right) + fu'v'$$
$$+ \frac{\tan\psi}{r}(u'v'\overline{u} + u'u'\overline{v} + u'u'v' - u'\overline{u'v'}) \quad \text{(A13)}$$

$$\frac{\partial}{\partial t}\left(\frac{1}{2}v'^2\right) = -\nabla_3 \cdot \mathbf{V}\frac{1}{2}v'^2 - v'\mathbf{V}' \cdot \nabla_3 \overline{v} - v'\overline{\nabla_3 \cdot \mathbf{V}' v'}$$
$$- \frac{v'}{r}\left(\frac{\partial \phi'}{\partial \psi}\right) - fu'v'$$
$$- \frac{\tan\psi}{r}(2u'v'\overline{u} + u'u'v' - v'\overline{u'u'}). \quad \text{(A14)}$$

Adding Eq. (A13) and (A14), defining $K_e = (1/2)u'^2 + (1/2)v'^2$, and simplifying gives

$$\frac{\partial}{\partial t}K_e = -\nabla_3 \cdot \mathbf{V}K_e - \mathbf{V}'_{\mathbf{h}} \cdot (\mathbf{V}' \cdot \nabla_3)\overline{\mathbf{V}}_{\mathbf{h}} - u'\overline{\nabla_3 \cdot \mathbf{V}' u'}$$
$$- v'\overline{\nabla_3 \cdot \mathbf{V}' v'} - \mathbf{V}'_{\mathbf{h}} \cdot \nabla_h \phi'$$
$$+ \frac{\tan\psi}{r}(u'u'\overline{v} - u'v'\overline{u} - u'\overline{u'v'} + v'\overline{u'u'}), \quad \text{(A15)}$$

where the subscript **h** denotes a vector with components in the horizontal dimensions only. The fifth term on the right-hand side of (A15), $-\mathbf{V}'_{\mathbf{h}} \cdot \nabla_h \phi'$, can be written as

$$-\nabla_h \cdot \mathbf{V}'_{\mathbf{h}} \phi' + \phi'(\nabla_h \cdot \mathbf{V}'_{\mathbf{h}}). \quad \text{(A16)}$$

Recognizing that $\nabla_h \cdot \mathbf{V}'_{\mathbf{h}} = -(\partial\omega'/\partial P)$ through continuity, (A16) becomes

$$-\nabla_h \cdot \mathbf{V}'_{\mathbf{h}} \phi' + \phi'\left(-\frac{\partial \omega'}{\partial P}\right). \quad \text{(A17)}$$

In turn, (A17) can be written as

$$-\nabla_h \cdot \mathbf{V}'_{\mathbf{h}} \phi' - \frac{\partial}{\partial P}\phi'\omega' + \omega'\frac{\partial \phi'}{\partial P},$$

which is equivalent to

$$-\nabla_3 \cdot \mathbf{V}' \phi' + \omega'\frac{\partial \phi'}{\partial P}. \quad \text{(A18)}$$

Substitution of (A18) for the term $-\mathbf{V}'_{\mathbf{h}} \cdot \nabla_h \phi'$ in (A15) yields

$$\frac{\partial}{\partial t}K_e = -\nabla_3 \cdot \mathbf{V}K_e - \mathbf{V}'_{\mathbf{h}} \cdot (\mathbf{V}' \cdot \nabla_3)\overline{\mathbf{V}}_{\mathbf{h}} - u'\overline{\nabla_3 \cdot \mathbf{V}' u'}$$
$$- v'\overline{\nabla_3 \cdot \mathbf{V}' v'} - \nabla_3 \cdot \mathbf{V}' \phi' + \omega'\frac{\partial \phi'}{\partial P}$$
$$+ \frac{\tan\psi}{r}(u'u'\overline{v} - u'v'\overline{u} - u'\overline{u'v'} + v'\overline{u'u'}). \quad \text{(A19)}$$

A friction term for the right-hand side of (A19) can be derived from the relations

$$\frac{\partial u}{\partial t} = \frac{1}{\rho}\frac{\partial \tau_u}{\partial z} \quad \text{(A20)}$$

$$\frac{\partial v}{\partial t} = \frac{1}{\rho}\frac{\partial \tau_v}{\partial z}, \quad \text{(A21)}$$

where τ_u (τ_v) is the aerodynamic stress in the zonal (meridional) direction due to unresolved processes. Terms related to horizontal derivatives in aerodynamic stress also could be represented on the right-hand side of (A20) and (A21). However, on the global reanalyses' relatively coarse latitude–longitude grid these terms scale to be quite small in comparison to the vertical derivative terms and so are not explicitly represented. The isobaric coordinate counterparts to (A20) and (A21) are

$$\frac{\partial u}{\partial t} = \frac{1}{\rho}\frac{\partial \tau_u}{\partial P}\frac{\partial P}{\partial z} \tag{A22}$$

$$\frac{\partial v}{\partial t} = \frac{1}{\rho}\frac{\partial \tau_v}{\partial P}\frac{\partial P}{\partial z}. \tag{A23}$$

With the hydrostatic approximation, (A22) and (A23) can be written as

$$\frac{\partial u}{\partial t} = -g\frac{\partial \tau_u}{\partial P} \tag{A24}$$

$$\frac{\partial v}{\partial t} = -g\frac{\partial \tau_v}{\partial P}. \tag{A25}$$

Partitioning u, v, τ_u, and τ_v into time-mean and instantaneous components and subtracting the time-mean components leaves

$$\frac{\partial u'}{\partial t} = -g\frac{\partial \tau_u'}{\partial P} \tag{A26}$$

$$\frac{\partial v'}{\partial t} = -g\frac{\partial \tau_v'}{\partial P}. \tag{A27}$$

Multiplying (A26) by u' and (A27) by v' and adding the resulting equations yields

$$\frac{\partial}{\partial t}K_e = -g\mathbf{V}_\mathbf{h}' \cdot \frac{\partial \boldsymbol{\tau}'}{\partial P} \tag{A28}$$

or, equivalently,

$$\frac{\partial}{\partial t}K_e = -g\frac{\partial}{\partial P}(\mathbf{V}_\mathbf{h}' \cdot \boldsymbol{\tau}') + g\boldsymbol{\tau}' \cdot \frac{\partial \mathbf{V}_\mathbf{h}'}{\partial P}. \tag{A29}$$

The right-hand side of (A29) can be included on the right-hand side of (A19), resulting in

$$\begin{aligned}\frac{\partial}{\partial t}K_e = {} & -\boldsymbol{\nabla}_3 \cdot \mathbf{V}K_e - \mathbf{V}_\mathbf{h}' \cdot (\mathbf{V}' \cdot \boldsymbol{\nabla}_3)\overline{\mathbf{V}}_\mathbf{h} - u'\overline{\boldsymbol{\nabla}_3 \cdot \mathbf{V}'u'} \\ & - v'\overline{\boldsymbol{\nabla}_3 \cdot \mathbf{V}'v'} - \boldsymbol{\nabla}_3 \cdot \mathbf{V}'\phi' + \omega'\frac{\partial \phi'}{\partial P} \\ & + \frac{\tan\psi}{r}(u'u'\overline{v} - u'v'\overline{u} - u'\overline{u'v'} + v'\overline{u'u'}) \\ & - g\frac{\partial}{\partial P}(\mathbf{V}_\mathbf{h}' \cdot \boldsymbol{\tau}') + g\boldsymbol{\tau}' \cdot \frac{\partial \mathbf{V}_\mathbf{h}'}{\partial P}.\end{aligned} \tag{A30}$$

The last term on the right-hand side of (A30) describes internal dissipation. It can be grouped into a residual term, the function of the residual being to account for all processes not explicitly represented on the right-hand side of (A30). Adding the residual to the right-hand side of (A30) and subsequently grouping the internal dissipation term into the residual yields

$$\begin{aligned}\frac{\partial}{\partial t}K_e = {} & -\boldsymbol{\nabla}_3 \cdot \mathbf{V}K_e - \mathbf{V}_\mathbf{h}' \cdot (\mathbf{V}' \cdot \boldsymbol{\nabla}_3)\overline{\mathbf{V}}_\mathbf{h} - u'\overline{\boldsymbol{\nabla}_3 \cdot \mathbf{V}'u'} \\ & - v'\overline{\boldsymbol{\nabla}_3 \cdot \mathbf{V}'v'} - \boldsymbol{\nabla}_3 \cdot \mathbf{V}'\phi' + \omega'\frac{\partial \phi'}{\partial P} \\ & + \frac{\tan\psi}{r}(u'u'\overline{v} - u'v'\overline{u} - u'\overline{u'v'} + v'\overline{u'u'}) \\ & - g\frac{\partial}{\partial P}(\mathbf{V}_\mathbf{h}' \cdot \boldsymbol{\tau}') + \text{res},\end{aligned} \tag{A31}$$

which is equivalent to Eq. (1) in section 3b of the body of the paper.

APPENDIX B

Calculation of the Residual Term

The residual at a particular analysis time t is defined as

$$\text{res}_t \equiv \frac{E_{t+12} - E_{t-12}}{2\Delta t} - \frac{D_{t-12} + 2D_t + D_{t+12}}{4}. \tag{B1}$$

Here $\Delta t = 12$ h (43 200 s), $t - 12$ ($t + 12$) denotes the time 12 h before (12 h after) t, and E_{t-12} (E_{t+12}) denotes the observed vertically averaged EKE at $t - 12$ ($t + 12$), obtained from the ECMWF reanalyses. Also, D_{t-12}, D_t, and D_{t+12} denote the diagnosed vertically averaged EKE tendency at times $t - 12$, t, and $t + 12$, respectively, obtained by the summation of terms b–i on the right-hand side of Eq. (1) in section 3b. The above definition of the residual has a finite-difference truncation error of $O(((1/2)\Delta t)^2)$. This is an improvement over the $O((\Delta t)^2)$ truncation error that would be incurred by defining the residual as

$$\text{res}_t \equiv \frac{E_{t+12} - E_{t-12}}{2\Delta t} - D_t. \tag{B2}$$

The improvement in truncation error arises from the fact that res_t, as given by the first definition above, is equivalent to

$$\frac{\text{res}_{t-6} + \text{res}_{t+6}}{2}, \tag{B3}$$

where

$$\text{res}_{t-6} = \frac{E_t - E_{t-12}}{\Delta t} - \frac{D_t + D_{t-12}}{2} + O\left[\left(\frac{1}{2}\Delta t\right)^2\right] \tag{B4}$$

$$\text{res}_{t+6} = \frac{E_{t+12} - E_t}{\Delta t} - \frac{D_{t+12} + D_t}{2} + O\left[\left(\frac{1}{2}\Delta t\right)^2\right]. \tag{B5}$$

REFERENCES

Balasubramanian, G., and M. K. Yau, 1996: The life cycle of a simulated marine cyclone: Energetics and PV diagnostics. *J. Atmos. Sci.*, **53,** 639–653.

Berbery, E. H., and C. S. Vera, 1996: Characteristics of the Southern

Hemisphere winter storm track with filtered and unfiltered data. *J. Atmos. Sci.,* **53,** 468–481.
Chang, E. K. M., 1993: Downstream development of baroclinic waves as inferred from regression analysis. *J. Atmos. Sci.,* **50,** 2038–2053.
——, 2000: Wave packets and life cycles of troughs in the upper troposphere: Examples from the Southern Hemisphere summer season of 1984/85. *Mon. Wea. Rev.,* **128,** 25–50.
——, and I. Orlanski, 1993: On the dynamics of a storm track. *J. Atmos. Sci.,* **50,** 999–1015.
——, and ——, 1994: On energy flux and group velocity of waves in baroclinic flows. *J. Atmos. Sci.,* **51,** 3823–3828.
——, and D. B. Yu, 1999: Characteristics of wave packets in the upper troposphere. Part I: Northern Hemisphere winter. *J. Atmos. Sci.,* **56,** 1708–1728.
Davies, H. C., C. Schär, and H. Wernli, 1991: The palette of fronts and cyclones within a baroclinic wave development. *J. Atmos. Sci.,* **48,** 1666–1689.
Hobbs, P. V., J. D. Locatelli, and J. E. Martin, 1996: A new conceptual model for cyclones generated in the lee of the Rocky Mountains. *Bull. Amer. Meteor. Soc.,* **77,** 1169–1178.
James, I. N., 1987: Suppression of baroclinic instability in horizontally sheared flows. *J. Atmos. Sci.,* **44,** 3710–3720.
——, and L. J. Gray, 1986: Concerning the effect of surface drag on the circulation of a baroclinic planetary atmosphere. *Quart. J. Roy. Meteor. Soc.,* **112,** 1231–1250.
Kreitzberg, C. W., 1968: The mesoscale wind field in an occlusion. *J. Appl. Meteor.,* **7,** 53–67.
Kung, E. C., 1977: Energy sources in middle-latitude synoptic-scale disturbances. *J. Atmos. Sci.,* **34,** 1352–1365.
Lackmann, G. M., D. Keyser, and L. F. Bosart, 1999: Energetics of an intensifying jet streak during the Experiment on Rapidly Intensifying Cyclones over the Atlantic (ERICA). *Mon. Wea. Rev.,* **127,** 2777–2795.
Lee, S., and I. M. Held, 1993: Baroclinic wave packets in models and observations. *J. Atmos. Sci.,* **50,** 1413–1428.
Lorenz, E. N., 1955: Available potential energy and the maintenance of the general circulation. *Tellus,* **VII,** 157–167.
Lott, F., 1995: Comparison between the orographic response of the ECMWF model and the PYREX 1990 data. *Quart. J. Roy. Meteor. Soc.,* **121,** 1323–1348.
Mak, M., 2000: Does an unstable baroclinic wave equilibrate/decay baroclinically or barotropically? *J. Atmos. Sci.,* **57,** 453–463.
——, and M. Cai, 1989: Local barotropic instability. *J. Atmos. Sci.,* **46,** 3289–3311.
Marsili, N., 2001: Rapid surface cyclolysis in the North Pacific Ocean: Structure and evolution of composite and individual case studies. M.S. thesis, Dept. of Atmospheric and Oceanic Sciences, University of Wisconsin—Madison, 181 pp. [Available from Department of Atmospheric and Oceanic Sciences, University of Wisconsin—Madison, 1225 W. Dayton St., Madison, WI 53706.]
Martin, J. E., 1998: The structure and evolution of a continental winter cyclone. Part I: Frontal structure and the occlusion process. *Mon. Wea. Rev.,* **126,** 303–328.
——, 1999: Quasigeostrophic forcing of ascent in the occluded sector of cyclones and the trowal airstream. *Mon. Wea. Rev.,* **127,** 70–88.
——, R. D. Grauman, and N. Marsili, 2001: Surface cyclolysis in the North Pacific Ocean. Part I: A synoptic climatology. *Mon. Wea. Rev.,* **129,** 748–765.
Masters, S. E., and E. C. Kung, 1986: An energetics analysis of cyclonic development in the Asian winter monsoon. *J. Meteor. Soc. Japan,* **64,** 35–51.
Nakamura, N., 1993: Momentum flux, flow symmetry, and the nonlinear barotropic governor. *J. Atmos. Sci.,* **50,** 2159–2179.
Orlanski, I., and J. Katzfey, 1991: The life cycle of a cyclone wave in the Southern Hemisphere. Part I: Eddy energy budget. *J. Atmos. Sci.,* **48,** 1972–1998.
——, and E. K. M. Chang, 1993: Ageostrophic geopotential fluxes in downstream and upstream development of baroclinic waves. *J. Atmos. Sci.,* **50,** 212–225.
——, and J. P. Sheldon, 1993: A case of downstream baroclinic development over western North America. *Mon. Wea. Rev.,* **121,** 2929–2950.
——, and ——, 1995: Stages in the energetics of baroclinic systems. *Tellus,* **47A,** 605–628.
——, and B. Gross, 2000: The life cycle of baroclinic eddies in a storm track environment. *J. Atmos. Sci.,* **57,** 3498–3513.
Palmen, E., 1951: The aerology of extratropical disturbances. *Compendium of Meteorology,* T. F. Malone, Ed. Amer. Meteor. Soc., 599–620.
Penner, C. M., 1955: A three-front model for synoptic analysis. *Quart. J. Roy. Meteor. Soc.,* **81,** 89–91.
Reed, R. J., 1979: Cyclogenesis in polar air streams. *Mon. Wea. Rev.,* **107,** 38–52.
Robertson, F. R., and P. J. Smith, 1980: The kinetic energy budgets of two severe storm producing extratropical cyclones. *Mon. Wea. Rev.,* **108,** 127–143.
Schultz, M. A., and C. F. Mass, 1993: The occlusion process in a midlatitude cyclone over land. *Mon. Wea. Rev.,* **121,** 918–940.
Shapiro, M. A., and D. Keyser, 1990: Fronts, jet streams, and the tropopause. *Extratropical Cyclones: The Erik Palmén Memorial Volume,* C. W. Newton and E. O. Holopainen, Eds., Amer. Meteor. Soc., 167–191.
Simmons, A. J., and B. J. Hoskins, 1978: The life cycles of some nonlinear baroclinic waves. *J. Atmos. Sci.,* **35,** 414–432.
——, and ——, 1980: Barotropic influences on the growth and decay of nonlinear baroclinic waves. *J. Atmos. Sci.,* **37,** 1679–1684.
Simons, T. J., 1972: The nonlinear dynamics of cyclone waves. *J. Atmos. Sci.,* **29,** 38–52.
Smith, P. J., 1973: The kinetic energy budget over North America during a period of major cyclone development. *Tellus,* **25,** 411–423.
Thorncroft, C. D., B. J. Hoskins, and M. E. McIntyre, 1993: Two paradigms of baroclinic-wave life-cycle behavior. *Quart. J. Roy. Meteor. Soc.,* **119,** 17–55.